

Contents lists available at ScienceDirect

Comput. Methods Appl. Mech. Engrg.

journal homepage: www.elsevier.com/locate/cma





Representing model uncertainties in brittle fracture simulations

Hao Zhang a, John E. Dolbow b, Johann Guilleminot a,*

- ^a Department of Civil and Environmental Engineering, Duke University, Durham, NC 27708, USA
- ^b Department of Mechanical Engineering and Materials Science, Duke University, Durham, NC 27708, USA

ARTICLE INFO

Keywords:
Phase-field modeling
Model uncertainty
Reduced-order modeling
Stiefel manifold
Uncertainty quantification

ABSTRACT

This work focuses on the representation of model-form uncertainties in phase-field models of brittle fracture. Such uncertainties can arise from the choice of the degradation function for instance, and their consideration has been unaddressed to date. The stochastic modeling framework leverages recent developments related to the analysis of nonlinear dynamical systems and relies on the construction of a stochastic reduced-order model. In the latter, a POD-based reduced-order basis is randomized using Riemannian projection and retraction operators, as well as an information-theoretic formulation enabling proper concentration in the convex hull defined by a set of model proposals. The model thus obtained is mathematically admissible in the almost sure sense and involves a low-dimensional hyperparameter, the calibration of which is facilitated through the formulation of a quadratic programming problem. The relevance of the modeling approach is further assessed on one- and two-dimensional applications. It is shown that model uncertainties can be efficiently captured and propagated to macroscopic quantities of interest. An extension based on localized randomization is also proposed to handle the case where the forward simulation is highly sensitive to sample localization. This work constitutes a methodological development allowing phase-field predictions to be endowed with statistical measures of confidence, accounting for the variability induced by modeling choices.

1. Introduction

The phase-field approach has become a predominant technique to simulate crack initiation, growth, merging and branching in complex materials. In this approach, a crack is approximated using a regularized, or diffuse, representation involving a continuous scalar field, referred to as the damage field [1,2]. Values for the later range from zero to one, where a zero value corresponds to intact material, and nonzero values indicate damaged material. This continuous description facilitates implementation using the conventional finite element method and does not require additional numerical treatment. This important feature is a key advantage of the method as compared with sharp crack models, which typically require specific remeshing techniques (see [3] for example) and/or *ad hoc* criteria for evolving the crack geometry (see, e.g., [4] for a review). Applications of the phase-field approach to brittle fracture modeling [5,6] are numerous and cannot be listed in an exhaustive manner; see, e.g., [7] for the design of composite materials, [8] for an application to biomaterials, and [9] for hydraulic fracturing simulations. Extensions to other setups can be found in [10–12] for ductile fracture, [13–15] for cohesive fracture, and [16–18] for dynamic fracture. Comprehensive reviews of the phase-field approach can be found in [19–21].

The complexity of the involved multiscale phenomena, together with the sensitivity of the predictions with respect to modeling choices and underlying physical parameters, calls for the development of uncertainty quantification (UQ) methodologies endowing

E-mail address: johann.guilleminot@duke.edu (J. Guilleminot).

^{*} Corresponding author.

predictions with appropriate measures of confidence (see [22,23] for reviews). Examples of modeling choices that are known to impact results in the strain-softening regime include the definition of the degradation function, which governs how developing damage affects the strain energy density of the healthy material, and the energy split scheme that ensure mechanical consistency in terms of crack propagation. Possible degradation functions include the widely used quadratic form [2], as well as the cubic function [24], the quartic function [25], the rational function [26], and the exponential function [27]; see, e.g., [28–32] for discussions. Similarly, possible split schemes include the volumetric–deviatoric and spectral decompositions, as well as variations thereof [33,34].

Most of the works integrating UQ components with phase-field modeling have focused on the description and propagation of parametric uncertainties, which are uncertainties affecting parameters in models that are assumed to be accurate. For example, the work in [35] studied the influence of uncertainties in various material parameters on the fracture toughness of polymeric clay nanocomposites; in [33], the authors developed and calibrated stochastic models capturing the spatial variations of the energy release rate and the critical fracture energy based on the morphology of the resulting crack patterns; the contribution in [36] studied the stochastic distribution of inclusions on the fracture performance of a rubber composite material, and uncertainties in elastic parameters were modeled using an *ad hoc* multiscale analysis in [37]. In a slightly different context, the work in [38] studied the influence of the spatial variability induced by the random initial packing of particles on the fracture of the particle monolayer raft driven by the interaction with surfactant. The Bayesian approach was employed in the context of parameter identification in [39,40] for brittle fracture, and in [41] for ductile material. Further studies focusing on parametric uncertainties in phase-field fracture simulations can be found in [42–45].

In contrast, the representation of model-form uncertainties to capture operator misspecification has received little to no attention to date. This lack of methodological developments mostly stems from the fact that model uncertainties do not naturally lend themselves to randomization, due to the functional nature of the problem. The objective of this work is to bridge this gap and develop a stochastic framework enabling the computationally efficient integration of model-form uncertainties in brittle fracture simulations. To this end, we leverage the approach developed in [46] to capture operator uncertainties in a multi-model discrete setting. Following the methodology proposed in [47] (see [48–50] for various applications), the approach relies on the randomization of a reduced-order basis, which is used to encode model information. The proposed strategy departs from [47] in the recourse to Riemannian operators mapping to and from the underlying manifold, which results in the construction of an alternative probabilistic model. This new formulation has key advantages, including the intrinsic satisfaction of linear constraints, a low stochastic dimension, ease of implementation and propagation, and facilitated inference. In this work, we extend the stochastic reduced-order modeling approach to the case of continuous systems (i.e., systems described by partial differential equations) and specifically, to brittle fracture simulations.

The remainder of the paper is laid out as follows. Section 2 provides necessary background on the phase-field approach to brittle fracture. The stochastic modeling framework is then introduced in Section 3, including reduced-order models for displacement and phase-field problems, and the stochastic representation. Numerical results are presented in Section 4. Several cases are considered to demonstrate the performance of the approach, including one- and two-dimensional applications under tensile and shear loading. Concluding remarks are finally provided in the last section.

2. Phase-field approach to brittle fracture

2.1. Brief review of the formulation

Consider a domain $\Omega \subset \mathbb{R}^m$ with boundary $\partial \Omega$, occupied by a brittle material characterized by a strain energy density function denoted by Ψ . The total potential energy \mathcal{E} is then defined as

$$\mathcal{E}(\boldsymbol{u},\Gamma) = \int_{\Omega \setminus \Gamma} \Psi(\boldsymbol{u}) \, dV - \int_{\partial \Omega_N} \bar{\boldsymbol{t}} \cdot \boldsymbol{u} \, dA + \int_{\Gamma} G_c \, dH^{m-1} \,, \tag{1}$$

where \pmb{u} denotes the displacement, Γ is the crack surface set, $\bar{\pmb{t}}$ is the field of external forces acting on the Neumann boundary $\partial\Omega_N$, G_c is the critical energy release rate (or fracture toughness), and dH^{m-1} denotes the Hausdorff measure. Additional boundary conditions $\pmb{u} = \bar{\pmb{u}}$ are prescribed on the Dirichlet boundary $\partial\Omega_D$, with $\partial\Omega_D\cap\partial\Omega_N=\emptyset$. In the phase field approach to brittle fracture, the above total energy is approximated as

$$\tilde{\mathcal{E}}(\boldsymbol{u},d;\ell) = \int_{\Omega} g(d)\Psi(\boldsymbol{u}) \, dV - \int_{\partial\Omega_N} \bar{\boldsymbol{t}} \cdot \boldsymbol{u} \, dA + \int_{\Omega} G_c \gamma(d,\nabla d) \, dV \,, \tag{2}$$

where d is the phase-field variable (taking values in [0,1]), usually interpreted (and referred to) as the damage field, ℓ is a regularization length, g is the degradation function that defines how damage modifies the stiffness of the healthy material, and γ denotes the crack surface density function. Here we employ the so-called AT2 model given by

$$\gamma(d, \nabla d) = \frac{1}{2} \left[\frac{1}{\ell} d^2 + \ell \nabla d \cdot \nabla d \right], \tag{3}$$

and note that an AT1 model could be used as well without significant impacts on the proposed developments. The energy $\tilde{\mathcal{E}}$ converges to \mathcal{E} as $\mathcal{E} \to 0$, in the sense of Γ -convergence. This setting gives rise to a diffuse representation of damage, as depicted in Fig. 1. To account for compression and tensile stress states, an additive split is typically introduced in the strain energy density function, so

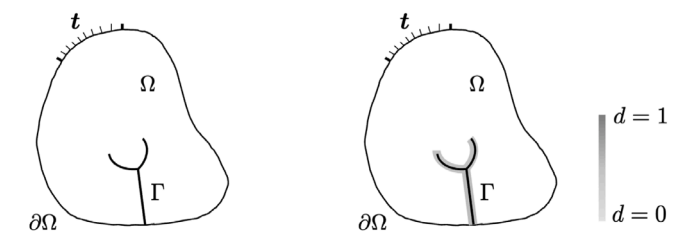


Fig. 1. Schematic representation of the smeared representation of cracks obtained in the phase-field setting.

that damage only affects the tensile component. This is formally accomplished by replacing the first term in the right-hand side in Eq. (2) by

$$\int_{\Omega} \left[g(d) \Psi^{+}(\mathbf{u}) + \Psi^{-}(\mathbf{u}) \right] dV \tag{4}$$

where Ψ^+ and Ψ^- denote the tensile and compression components of Ψ , respectively. Several choices pertaining to the definition of these components were proposed in the literature, including the volumetric-deviatoric [51] and spectral [52] decompositions. The later is adopted in this work, without loss of generality in terms of the stochastic modeling components. Assuming isotropy for the intact material, one has

$$\Psi^{\pm} = \frac{1}{2} \lambda \langle \text{tr}([\varepsilon]) \rangle_{\pm}^{2} + \mu[\varepsilon^{\pm}] : [\varepsilon^{\pm}], \tag{5}$$

where λ and μ are the Lamé constants, $[\varepsilon^{\pm}] = \sum_{i=1}^{m} \langle \varepsilon_i \rangle_{\pm} \, p_i \otimes p_i$, ε_i and p_i denote the principal strains and the corresponding eigenvectors of the strain tensor $[\varepsilon] = \frac{1}{2} (\nabla u + \nabla^T u)$, respectively, and $\langle a \rangle_{\pm} = \frac{1}{2} (a \pm |a|)$. The pair of solution fields $\{u,d\}$ can be determined by minimizing

$$\arg \min_{\boldsymbol{u},d} \int_{\Omega} g(d) \Psi^{+}(\boldsymbol{u}) \, dV + \int_{\Omega} \Psi^{-}(\boldsymbol{u}) \, dV - \int_{\partial \Omega_{N}} \bar{t} \cdot \boldsymbol{u} \, dA + \int_{\Omega} G_{c} \gamma(d, \nabla d) \, dV,$$
subject to $\dot{d} \geq 0$, (6)

where the inequality constraint reflects the irreversibility of the damage process.

Rather than seeking a true minimizer, in this work we consider the approximation introduced by [52] in which the governing equations are given by

$$\nabla \cdot [\sigma] = 0 \text{ in } \Omega, \tag{7}$$

$$\frac{G_c}{\mathscr{L}}(d-\mathscr{L}^2\nabla^2 d) + g'(d)\mathcal{H} = 0 \text{ in } \Omega,$$
(8)

together with the boundary conditions

$$[\sigma] \cdot \mathbf{n} = \bar{\mathbf{t}} \text{ on } \partial \Omega_N,$$
 (9)

$$\nabla d \cdot \mathbf{n} = 0 \text{ on } \partial \Omega$$
, (10)

where \mathcal{H} is the monotonic driving force

$$\mathcal{H}(\mathbf{x},t) = \max_{\tau \in [0,t]} \Psi^{+}([\varepsilon(\mathbf{x},\tau)]), \tag{11}$$

introduced to enforce the monotonicity constraint $\dot{d} > 0$, and n is the outward-pointing unit vector normal to the boundary under consideration. The damage degraded stress tensor $[\sigma]$ is related to the infinitesimal strain tensor through the constitutive equation

$$[\sigma] = g(d)\frac{d\Psi^{+}}{d[\varepsilon]} + \frac{d\Psi^{-}}{d[\varepsilon]}.$$
 (12)

The displacement problem is nonlinear due to the tensile-compression split, and the phase-field problem is also generally nonlinear (except for specific choices of the degradation function). In order to accelerate computations, and given the scope of (and applications retained for) the proposed contribution, the hybrid formulation proposed in [21] is employed hereafter. In this formulation, the displacement problem is solved without split, implying that the stress tensor is degraded according to

$$[\sigma] = g(d) \left(\lambda \operatorname{tr}([\varepsilon])[I_m] + 2\mu[\varepsilon] \right), \tag{13}$$

where $[I_m]$ is the identity matrix of dimension m, and the phase-field problem is solved with the spectral decomposition.

2.2. Approximation by the finite element method

In this work, the solution to the coupled displacement and phase-field problems is sought using the staggered scheme proposed in [52] and the finite element method. Some aspects of this strategy are briefly reviewed below to lay the ground for the introduction of the stochastic reduced-order formulation, presented in Section 3. Note that the reduced-order model will be applied either to the displacement or to the phase-field problem, hence the use of similar notation within the next two sections.

2.2.1. Displacement problem

The trial and weighting spaces for the displacement field are defined as $\mathcal{U} = \{ \boldsymbol{u} \in H^1(\Omega), \ \boldsymbol{u} = \overline{\boldsymbol{u}} \text{ on } \partial\Omega_D \}$ and $\mathcal{U}_0 = \{ \boldsymbol{v} \in H^1(\Omega), \ \boldsymbol{v} = 0 \text{ on } \partial\Omega_D \}$, respectively. The derivation of the weak and Galerkin forms of the problem, at given boundary displacement increment and fixed-point iteration, is standard and can be found in, e.g., [19]. Considering a finite element mesh with N nodes, the linear system is written as

$$[K_{\nu}]\hat{u} = F_{\nu}, \tag{14}$$

where $[K_u]$ is the global stiffness matrix, $\hat{u} \in \mathbb{R}^{mN}$ denotes the vector of nodal displacements, and F_u is the global force vector. At any increment and iteration, the vector of nodal values satisfies the linear constraints equation

$$[B_u]^T \hat{\boldsymbol{u}} = \boldsymbol{0}_{N_{CD}} \,, \tag{15}$$

where $[B_u] \in \mathbb{R}^{mN \times N_{CD}}$ reflects homogeneous Dirichlet boundary conditions and satisfies $[B_u]^T[B_u] = [I_{N_{CD}}]$, $\mathbf{0}_{N_{CD}}$ is the null vector of length N_{CD} , and N_{CD} is the number of vanishing displacement components.

2.2.2. Phase-field problem

The trial and weighting spaces for the phase-field variable are defined as $\mathcal{V} = \{d \in H^1(\Omega), \ d=1 \text{ on } \Gamma_0\}$ and $\mathcal{V}_0 = \{w \in H^1(\Omega), \ w=0 \text{ on } \Gamma_0\}$, respectively, with Γ_0 the initial notch. As previously indicated, the phase-field problem is generally nonlinear and is typically solved using the Newton–Raphson method; see [19] for discussions and derivations of the Galerkin approximation. The nonlinear problem can be written as

$$K_d(\hat{d}) = F_d$$
, (16)

where K_d denotes the nonlinear operator arising from the weak formulation, \hat{d} is the vector of nodal values for the phase-field variable, and F_d denotes the global force vector. The solution satisfies a set of linear constraints, written in matrix form as

$$[B_d]^T (\hat{\boldsymbol{d}} - \boldsymbol{d}_0) = \boldsymbol{0}_{N_{CD}} \tag{17}$$

at any displacement increment and iteration, where $[B_d] \in \mathbb{R}^{N \times N_{CD}}$ satisfies $[B_d]^T [B_d] = [I_{N_{CD}}]$, N_{CD} is the number of constrained degrees of freedom for the phase-field problem, and $d_0 \in \mathbb{R}^N$ is such that $(d_0)_i = 1$ if the ith node is located on the initial notch Γ_0 , and $(d_0)_i = 0$ otherwise. At a given load increment, let $\widehat{\boldsymbol{d}}^{(0)}$ be the solution initial guess and let $\boldsymbol{r}^{(k)} = K_d(\widehat{\boldsymbol{d}}^{(k)}) - \boldsymbol{F}_d^{(k)}$ be the residual vector at kth iteration. The approach then consists in constructing the sequence $\{\widehat{\boldsymbol{d}}^{(k)}\}_{k>0}$ of approximations where

$$\widehat{\boldsymbol{d}}^{(k+1)} = \widehat{\boldsymbol{d}}^{(k)} + \Delta \widehat{\boldsymbol{d}}^{(k)} \tag{18}$$

and the increment $\Delta \hat{\boldsymbol{d}}^{(k)}$ is evaluated by solving the linear system

$$[T^{(k)}]\Delta\hat{\boldsymbol{d}}^{(k)} = -\boldsymbol{r}^{(k)}. \tag{19}$$

where $[T_d^{(k)}] = \partial K(\hat{\boldsymbol{d}}^{(k)})/\partial \hat{\boldsymbol{d}}^{(k)}$ denotes the symmetric positive-definite tangent matrix. Note that the increment also satisfies the set of linear constraints

$$[B_d]^T \Delta \hat{\boldsymbol{d}}^{(k)} = \boldsymbol{0}_{N_{CD}} \tag{20}$$

at any iteration.

2.3. Model-form uncertainties arising from the choice of degradation functions

The degradation function g induces a coupling between the displacement and damage fields. It therefore plays a crucial role in the phase-field approach to brittle fracture modeling. This function is required to satisfy the following constraints:

- 1. Values at d = 0 and d = 1 are prescribed to g(0) = 1 and g(1) = 0, respectively;
- 2. The function g is non-increasing in the interval [0,1], i.e., $g'(d) \le 0$ for $d \in [0,1]$;
- 3. The derivative at d = 1 vanishes to force the driving force term g'H to be zero when fracture incurs.

The quadratic degradation function

$$g_2(d) = (1-d)^2$$
 (21)

is arguably the most widely used degradation function [2] as it ultimately leads to a linear formulation for the phase-field problem and presents good modeling capabilities [14,53]. Other functions were proposed in the literature to model a variety of materials, including

• the cubic function [24]: $g_3(d) = (3-s)(1-d)^2 - (2-s)(1-d)^3$;

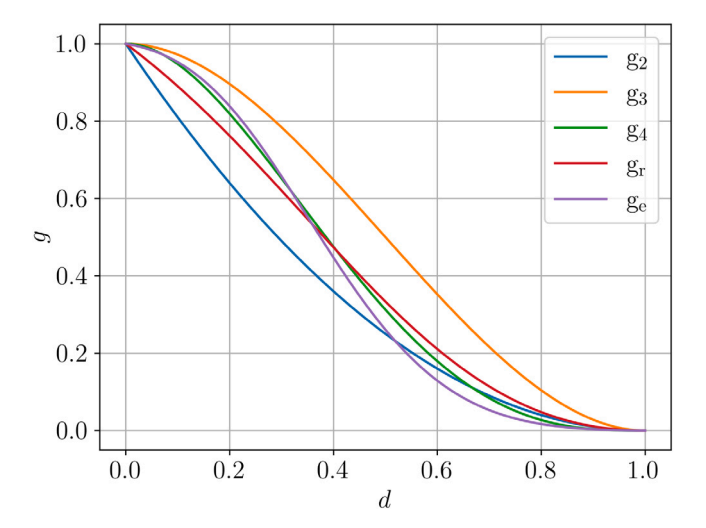


Fig. 2. Plot of the degradation functions $d \mapsto g_i(d)$ for $i \in \{2, 3, 4, r, e\}$. Here, $s = 1 \times 10^{-4}$ for g_3 , $a_1 = 0.5$ and p = 1.0 for g_r , w = 0.1 and $\alpha = 3.0$ (with other parameters solved for as functions of w and α ; see Sections 5.2 and 5.3 in [27]) for g_r .

- the quartic function [25]: $g_4(d) = 4(1-d)^3 3(1-d)^4$;
- the rational function [26]:

$$g_r(d) = \frac{(1-d)^2}{(1-d)^2 + (a_1d + a_1pd^2)} \; ;$$

• the exponential-type function [27]:

$$g_e(d) = (1 - w) \frac{1 - \exp(-k(1 - d)^{\alpha})}{1 - \exp(-k)} + w f_c(d), \quad f_c(d) = a_2(1 - d)^2 + a_3(1 - d)^3.$$

The corresponding degradation functions are plotted in Fig. 2, for specific choices of model parameters. It can be seen that the different functional forms for the degradation function lead to different decay rates and behaviors at extreme damage values. This choice is known to impact the softening regime and therefore affects predictability. Without loss of methodological generality, we focus from now on the integration of such model-form uncertainties in phase-field fracture simulations. The consideration of other sources of uncertainties, including the impact of the split scheme, and integration within more recent phase-field formulations (such as the theory developed in [54] to account for nucleation), are left for future work. The stochastic modeling framework is introduced in the next section.

3. Stochastic modeling in phase-field fracture simulations

In this section, the stochastic modeling approach aiming to represent model-form uncertainties in the context of phase-field simulations is introduced. The framework involves reduced-order modeling where the model-encoding projection basis is randomized. Reduced-order models for the displacement and phase-field problems are first presented in Section 3.1. The probabilistic model is then detailed in Section 3.2.

3.1. Reduced-order modeling for phase-field simulations

The system of coupled equations reads as

$$\begin{cases} \nabla \cdot [\sigma] = 0, & \text{with } [\sigma] \cdot \mathbf{n} = \overline{\mathbf{i}} \text{ on } \partial \Omega_N, & \mathbf{u} = \overline{\mathbf{u}} \text{ on } \partial \Omega_D, \\ \frac{G_c}{\ell} (d - \ell^2 \nabla^2 d) + g'(d) \mathcal{H} = 0, & \text{with } \nabla d \cdot \mathbf{n} = 0 \text{ on } \partial \Omega, & d = 1 \text{ on } \Gamma_0. \end{cases}$$
(22)

The above equations are solved using a staggered scheme, using the hybrid formulation presented in [21] (i.e., without considering a split in the constitutive model for the displacement problem, and using a spectral decomposition in the phase-field equation). In the context of uncertainty quantification where variability is propagated in an iterative manner between the two governing equations (see Eq. (22)), a reduced-order model can be constructed for, and used as a means to randomize the operator in, any of the aforementioned problems. The construction of such models, which serves as the starting point of the methodology, is carried out in Sections 3.1.1 and 3.1.2.

3.1.1. Reduced-order modeling for the linear displacement problem

Many techniques can be deployed to construct a reduced-order basis. In this work, we use proper orthogonal decomposition (POD) due to ease of implementation and amenability for analysis; see [45,55–57] for contributions reporting on different reduced-order modeling approaches. Note that the use of an alternative method may lead to a lower-dimensional latent space, but does not modify the methodological and technical results put forward in this paper.

Let $[X_u]$ be the matrix containing the snapshots of the displacement vector at all iterations in the staggered scheme, for all displacement increments, and consider the singular value decomposition:

$$[X_n] = [U][S][V]^T$$
 (23)

The reduced-order basis $[\Phi_u] \in \mathbb{R}^{mN \times n}$ can be obtained by retaining the first n dominant eigenvectors of matrix [U]. The integer n can be determined by analyzing the convergence of the error function

$$\epsilon(r) = 1 - \frac{\sum_{i=1}^{r} [S]_{ii}^2}{\sum_{i=1}^{mN} [S]_{ii}^2}.$$
(24)

The number of modes n is chosen such that $\epsilon(r) < \overline{\epsilon}$ for r > n, where $\overline{\epsilon}$ is a user-specified application-dependent threshold. The reduced-order variable $\widetilde{u} \in \mathbb{R}^n$ is then defined as $\widetilde{u} = [\Phi_u]^T \widehat{u}$ and satisfies the reduced-order linear system

$$[\widetilde{K}_u]\widetilde{u} = \widetilde{F}_u, \tag{25}$$

where the reduced stiffness matrix and reduced force vector are defined as

$$[\widetilde{K}_{n}] = [\boldsymbol{\Phi}_{n}]^{T} [K_{n}] [\boldsymbol{\Phi}_{n}], \quad \widetilde{F}_{n} = [\boldsymbol{\Phi}_{n}]^{T} F_{n}, \tag{26}$$

respectively. Note that the reduced-order basis also satisfies the matrix equation

$$[B_u]^T [\Phi_u] = [0_{N_{CD,R}}],$$
 (27)

due to Eq. (15). Once the reduced-order linear system is solved, the approximated solution in physical space is obtained as $\hat{u} \approx [\Phi_u]\tilde{u}$.

3.1.2. Reduced-order modeling for the nonlinear phase-field problem

The reduced-order model for the phase-field problem is similarly derived using POD. Let $[X_d]$ be the matrix containing the snapshots of the damage nodal values at all loading increments and all iterations in the staggered scheme, and denote by $[\boldsymbol{\Phi}_d] \in \mathbb{R}^{N \times n}$ the associated reduced-order basis. For a given loading increment, let $\widetilde{\boldsymbol{d}}^{(0)} = [\boldsymbol{\Phi}_d]^T \widehat{\boldsymbol{d}}^{(0)}$ be the reduced initial guess, and consider the sequence $\{\widetilde{\boldsymbol{d}}^{(k)}\}_{k \geq 0}$, with $\widetilde{\boldsymbol{d}}^{(k+1)} = \widetilde{\boldsymbol{d}}^{(k)} + \Delta \widetilde{\boldsymbol{d}}^{(k)}$, where $\Delta \widetilde{\boldsymbol{d}}^{(k)} \in \mathbb{R}^n$ denotes the reduced increment satisfying

$$[\widetilde{T}^{(k)}]\Delta\widetilde{\boldsymbol{d}}^{(k)} = -\widetilde{\boldsymbol{r}}^{(k)}, \tag{28}$$

where $[\widetilde{T}^{(k)}] \in \mathbb{R}^{n \times n}$ is the reduced tangent matrix and $\widetilde{r}^{(k)} \in \mathbb{R}^n$ is the reduced residual vector:

$$[\widetilde{T}^{(k)}] = [\boldsymbol{\Phi}_d]^T [T^{(k)}] [\boldsymbol{\Phi}_d], \quad \widetilde{\boldsymbol{r}}^{(k)} = [\boldsymbol{\Phi}_d]^T \left(K_d ([\boldsymbol{\Phi}_d] \widetilde{\boldsymbol{d}}^{(k)}) \right) - F_d \left([\boldsymbol{\Phi}_d] \widetilde{\boldsymbol{d}}^{(k)} \right). \tag{29}$$

The reduced-order basis satisfies the matrix-form constraint

$$[B_d]^T[\Phi_d] = [0_{N_{CD},n}],$$
 (30)

in view of Eq. (20). The Newton–Raphson solver terminates once the norm of the residual falls below a given threshold, taken as 1×10^{-10} in this work. The physical damage field solution is approximated as $\hat{d} = [\Phi_d]\tilde{d}$, where \tilde{d} is the reduced-order solution obtained at convergence in the Newton–Raphson algorithm (for a given displacement loading).

3.2. Stochastic representation of reduced-order bases

Following [47], we seek to capture model-form uncertainties by randomizing either $[\Phi_u]$ or $[\Phi_d]$. Let $[\Phi]$ be the stochastic counterpart of any of these deterministic reduced-order bases, defined on a probability space (Θ, \mathcal{F}, P) . The following minimal set of constraints is considered:

- 1. The stochastic reduced-order basis $[\Phi]$ takes values in the Stiefel manifold St(N', n), with N' = mN;
- 2. The stochastic reduced-order basis $[\Phi]$ satisfies the constraint $[B]^T[\Phi] = [0_{N_{CD},n}]$ almost surely, where [B] denotes either $[B_u]$ or $[B_d]$ (depending on the setup);
- 3. The Fréchet mean of $[\Phi]$ can be prescribed.

It should be noticed that the first two constraints are necessary to ensure well-posedness, while the third property is desired to facilitate calibration. Leveraging the *multi-model* setting considered in this paper, we then follow the construction proposed in [46]. The approach relies on the use of Riemannian operators to develop models on the tangent space to the Stiefel manifold, and thus departs from the original strategy proposed in [47] (see [48,50] for applications) where the polar-decomposition was adopted for the *uni-model* setting.

Observe first that the space

$$\mathbb{S}_{N',n} = \{ [Y] \in \mathbb{R}^{N' \times n} \mid [Y]^T [Y] = [I_n], \quad [B][Y] = [0_{N_{CD},n}] \}$$
(31)

defines the support of the probability measure of $[\Phi]$. In order to operate on the tangent space

$$T_{[Y]}St(N',n) = \{ [\Delta] \in \mathbb{R}^{N' \times n}, [Y]^T [\Delta] + [\Delta]^T [Y] = [0_n] \}$$
 (32)

at basepoint $[Y] \in St(N', n)$, equipped with the canonical inner product

$$\langle [\Delta], [\widetilde{\Delta}] \rangle_{[Y]} = \operatorname{tr}([\Delta]^T ([I_{N'}] - \frac{1}{2} [Y][Y]^T) [\widetilde{\Delta}]) \tag{33}$$

and induced metric

$$\|[\underline{A}]\|_{[Y]} = \langle [\underline{A}], [\underline{A}] \rangle_{[Y]}^{1/2}, \tag{34}$$

consider the Riemannian projection operator

$$P_{[Y]}: St(N',n) \to T_{[Y]}St(N',n), \quad [\Delta] = P_{[Y]}([\widetilde{Y}]) = \log_{[Y]}^{St}([\widetilde{Y}]), \tag{35}$$

where $\log_{[Y]}^{S_t}$ is the Riemannian logarithm at basepoint [Y], and the Riemannian retraction operator

$$R_{[Y]}: T_{[Y]}St(N', n) \to St(N', n), \quad [\widetilde{Y}] = R_{[Y]}([\Delta]) = \exp_{[Y]}^{St}([\Delta]),$$
 (36)

where $\exp_{[Y]}^{St}$ is the Riemannian exponential operator. Specifically, we consider the Riemannian projection and retraction operators defined by Zimmermann in [58] (see Algorithms 7 and 8 there in for numerical schemes). We have shown in [46] that these operators preserve the action of the linear constraints, in the following sense:

- If $[Y] \in \mathbb{S}_{N',n}$ and $[\widetilde{Y}] \in \mathbb{S}_{N',n}$, then $P_{[Y]}([\widetilde{Y}]) \in \mathbb{S}_{N',n}$.
- If $[Y] \in \mathbb{S}_{N',n}$ and $[\Delta] \in \mathbb{S}_{N',n}$, then $R_{[Y]}([\Delta]) \in \mathbb{S}_{N',n}$.

Next, consider the set $\{[\Delta^{(i)}]\}_{i=1}^m$ defined as

$$[\Delta^{(i)}] = P_{(\phi)}([\Phi^{(i)}]), \quad 1 \le i \le m,$$
 (37)

where $[\Phi^{(i)}]$ is the reduced-order basis associated with the *i*th degradation function (recall that either the displacement or phase-field reduced-order model is considered, i.e., $[\Phi^{(i)}] = [\Phi_u^{(i)}]$ or $[\Phi^{(i)}] = [\Phi_d^{(i)}]$, and $[\underline{\Phi}]$ is the global reduced-order basis obtained by applying the POD procedure to the matrix containing all snapshots for all models (accordingly, $[\underline{\Phi}]$ denotes either $[\underline{\Phi}_u]$ or $[\underline{\Phi}_d]$). It then follows that

$$R_{[\underline{\Phi}]}\left(\sum_{i=1}^{m} p_{i}[\Delta^{(i)}]\right) \in \mathbb{S}_{N',n} \subset St(N',n), \quad \forall (p_{1},\ldots,p_{m})^{T} \in \mathbb{R}^{m},$$

$$(38)$$

by linearity. This result implies that it is, indeed, sufficient to randomize the coefficients $\{p_j\}_{j=1}^m$ in Eq. (38), and to apply the Riemannian retraction operator to ensure that the first two constraints listed at the beginning of this section are satisfied almost surely. Let $P = (P_1, \dots, P_m)^T$ denote the random vector of coefficients on the tangent space. The stochastic reduced-order basis defined as

$$[\boldsymbol{\Phi}] = \exp_{[\underline{\boldsymbol{\Phi}}]}^{St} \left\{ \sum_{i=1}^{m} P_i \log_{[\underline{\boldsymbol{\Phi}}]}^{St} ([\boldsymbol{\Phi}^{(i)}]) \right\}, \quad \boldsymbol{P} \sim \pi,$$
(39)

is then mathematically consistent almost surely, with π the underlying probability measure. When no additional information pertaining to, e.g., higher-order statistical moments or the structure of statistical fluctuation is available, a non-informative prior measure shall be selected. In particular, the use of a Dirichlet distribution with concentration parameters gathered in $\alpha = (\alpha_1, \dots, \alpha_m) \in \mathbb{R}^m$, i.e.,

$$P \sim D(\alpha)$$
, (40)

leads to a so-called stochastic Riemannian convex combination. The latter ensures that samples are generated within the convex hull of the reduced-order basis dataset on the Stiefel manifold. The procedure to generate samples of the reduced-order basis according to the above model is summarized in Alg. 1.

Algorithm 1 Procedure to generate one sample of the stochastic reduced-order basis.

Require: Concentration coefficient $\alpha = (\alpha_1, \dots, \alpha_m)$, global reduced-order basis $[\underline{\Phi}]$ (basepoint), reduced-order bases $[\Phi^{(1)}], \dots, [\Phi^{(m)}]$ corresponding to the m model proposals (for a given reduced-order model).

- 1: Compute $[\Delta^{(i)}] = \log_{[\Phi]}^{St}([\Phi^{(i)}])$, for i = 1, ..., m, using Algorithm 8 in [58].
- 2: Draw a sample $p(\theta_j) = (p_1(\theta_j), \dots, p_m(\theta_j))^T$ from $D(\alpha)$.
- 3: Compute the sample $[\Phi(\theta_j)] = \exp_{[\Phi]}^{St}(\sum_{i=1}^m p_i(\theta_j)[\Delta^{(i)}])$, using Algorithm 7 in [58].

Ensure: Sample of the stochastic reduced-order basis $[\Phi]$.

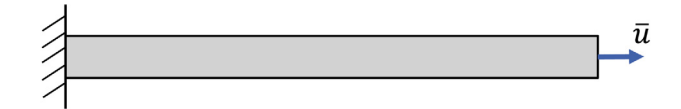


Fig. 3. One-dimensional bar domain. Left side is fixed, while tension is applied on the right side.

To deploy the stochastic reduced-order model, it is necessary to define the physical problem (i.e., the governing equations) associated with a new sample of the reduced-order basis, denoted by $[\Phi(\theta_j)]$ (and defined by the corresponding sample $p(\theta_j) = (p_1(\theta_j), \ldots, p_m(\theta_j))^T$ of the coefficients). One strategy consists in localizing the closest reduced-order basis in the dataset, and consider the problem parameterized by the corresponding parameters [46]. In other words, if $[\Phi(\theta_j)]$ is closer to, say, $[\Phi^{(2)}]$, using the canonical metric, then we shall use the degradation function g_2 and the associated regularization length, denoted by ℓ_2 for consistency. Another possible strategy relies on the observation that the convex combination

$$\hat{g}^{(j)}(d) = \sum_{i=1}^{m} p_i(\theta_j) g_i(d),$$
(41)

which is associated with the jth sample of the random vector P, is an admissible degradation function, since $\hat{g}^{(j)}(0) = 1$, $\hat{g}^{(j)}(1) = 0$, and $d \mapsto \hat{g}^{(j)}(d)$ is non-increasing by construction. Based on extensive numerical testing (not reported below for the sake of conciseness), the later approach was pursued in this work. In a similar manner, a convex combination was used for the regularization length $\ell^{(j)}$ for the physical model associated with sample $[\Phi(\theta_j)]$ (in lieu of the more conservative choice $\ell^{(j)} = \min(\ell_1, \dots, \ell_m)$). As previously indicated, it is desirable to localize fluctuations by prescribing the Fréchet mean of the stochastic reduced-order basis. This mean may be set to coincide with the global reduced-order basis, since the latter incorporates solution snapshots from all models, or the Fréchet mean of the dataset for instance. Consider the former for the sake of illustration, and without loss of generality:

$$\mathbb{E}\{\{\boldsymbol{\phi}\}\}\approx[\boldsymbol{\phi}].\tag{42}$$

It was shown in [46] that this can be achieved by defining the vector of concentration parameters as

$$\boldsymbol{\alpha} = \arg\min_{\boldsymbol{a} \in \mathbb{R}^m_{>0}} \| \sum_{i=1}^m a_i \log_{[\underline{\boldsymbol{\Phi}}]}^{St} ([\boldsymbol{\Phi}^{(i)}]) \|_F,$$

$$\tag{43}$$

which can be rewritten, with little algebra, as

$$\alpha = \arg\min_{a \in \mathbb{R}^m_{>0}} a^T[H]a, \tag{44}$$

where $[H] \in \mathbb{R}^{m \times m}$ is the symmetric positive-definite matrix with entries

$$H_{ij} = \text{tr} \left\{ \log_{|\Phi|}^{St} ([\Phi^{(i)}])^T \log_{|\Phi|}^{St} ([\Phi^{(j)}]) \right\}. \tag{45}$$

The above quadratic optimization problem only involves the reduced-order bases composing the initial dataset (i.e., those associated with the model proposals, here the set of possible degradation functions), and can be solved once for all prior to subsequent uncertainty quantification analyses.

4. Numerical applications

In all applications discussed below, the open-source computing platform FEniCS [59] was employed to solve the reduced-order phase-field fracture problems. For each application, a subset of degradation functions is selected based on the spread observed in the macroscopic response and convergence aspects.

4.1. One-dimensional application

4.1.1. Problem description

The stochastic reduced-order modeling of brittle fracture is first deployed in a one-dimensional setting, considering the bar shown in Fig. 3. The length of the bar is 20 [mm], the Young's modulus is $E=1\times10^6$ [N m⁻²], the fracture energy is $G_c=1\times10^3$ [J m⁻²]. The left end of the bar is fixed, while a Dirichlet boundary condition is imposed on the right end. The phase-field damage values are set to 0 on both ends so that fracture occurs in the middle of the bar. The loading \bar{u} is imposed on the right side with increments of 0.01 [mm] until the crack is generated. A discretization with element length of 0.01 [mm] is employed, resulting in a total number of 2501 nodes. In this particular setting, no tensile–compression split is applied in the strain energy density term (in the phase-field equation) given the pure tension state.

Four degradation functions are employed (m = 4), namely g_2 , g_4 , g_r , and g_e (see Section 2.3). Parameters in these functions are set as follows: $a_1 = 0.5$, p = 1 (in g_r), w = 0.1, and $\alpha = 4$ (in g_e). The corresponding regularization lengths are set to 0.2, 0.36,

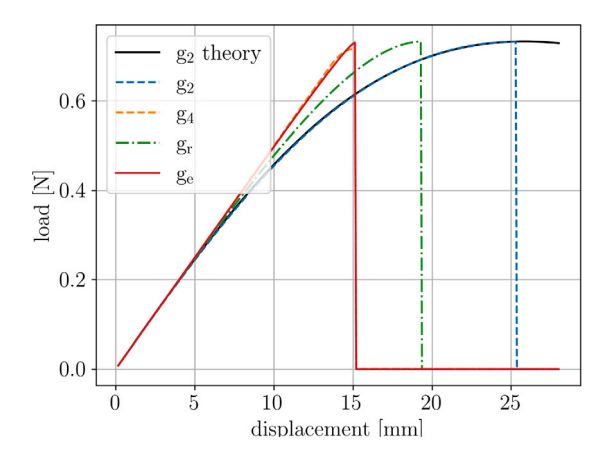


Fig. 4. The loading curve obtained using four different degradation functions (and different regularization lengths), together with the theoretical result using quadratic degradation function g_2 .

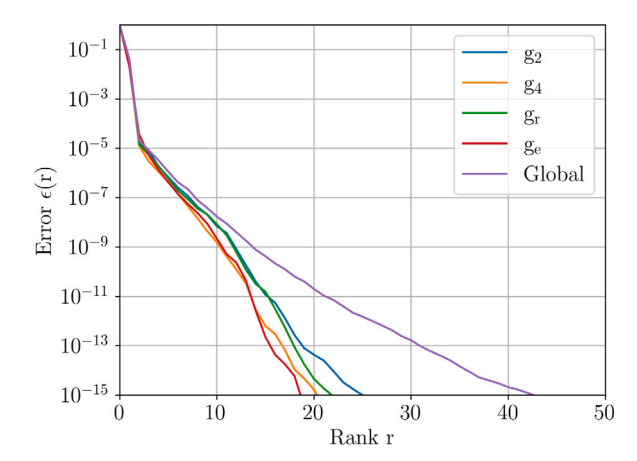


Fig. 5. Graph of the error function $r \mapsto \epsilon(r)$ (see Eq. (24)) for all models (reduced-order displacement equation). Recall that the global reduced-order basis is obtained by merging all solution snapshots for all models.

0.32, and 0.4 [mm], respectively, in order to match the peak stress. Note that in the case of the quadratic degradation function, the theoretical strain–stress response can be derived as [19]:

$$\sigma(\varepsilon) = \left(\frac{G_c}{G_c + \ell' E \varepsilon^2}\right)^2 E \varepsilon . \tag{46}$$

This theoretical result, together with the numerical results for all degradation functions, are shown in Fig. 4. It is seen that the theoretical response matches with the simulation result for the quadratic degradation function, which validates the accuracy of the numerical simulation. As expected, the choice of the degradation function results in large discrepancies in terms of the loading curves. In the next section, we employ the proposed stochastic framework to generate an ensemble of models that is consistent with this functional dataset. The randomization of the displacement problem is first addressed in Section 4.1.2. Application to the displacement problem is then presented in Section 4.1.3.

4.1.2. Stochastic simulations with reduced-order displacement equation

In this section, the stochastic reduced-order modeling approach is deployed on the displacement equation (see Section 3.1.1).

4.1.2.1. Computation of the nominal reduced-order bases. The POD approach is employed to calculate the reduced-order bases $\{[\boldsymbol{\phi}_u^{(1)}], [\boldsymbol{\phi}_u^{(2)}], [\boldsymbol{\phi}_u^{(3)}], [\boldsymbol{\phi}_u^{(4)}]\}$ associated with the degradation functions $\{g_2, g_4, g_r, g_e\}$, respectively, as well as the global reduced-order basis $[\underline{\boldsymbol{\Phi}}_u]$. Fig. 5 shows the graph of the error function defined by Eq. (24), for all scenarios. Setting the error threshold to $\overline{\epsilon} = 10^{-7}$, based on observed convergence in the load–displacement curve, ten modes are selected to build the reduced-order bases, leading to stochastic modeling in $\mathbb{S}_{2501,10} \subset St(2501,10)$.

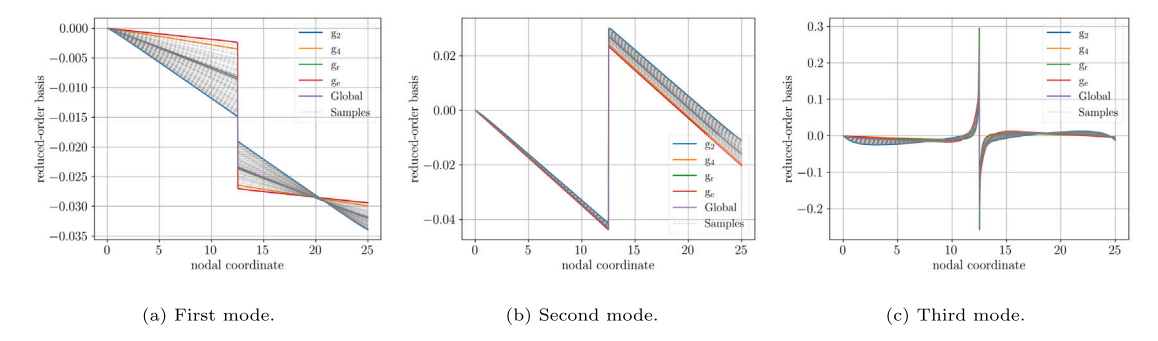


Fig. 6. First three modes of the initial reduced-order bases $[\Phi_u^1]$, $[\Phi_u^2]$, $[\Phi_u^3]$, and $[\Phi_u^4]$ (colored lines), and 100 additional samples (reduced-order displacement equation). (For interpretation of the references to color in this figure legend, the reader is referred to the web version of this article.)

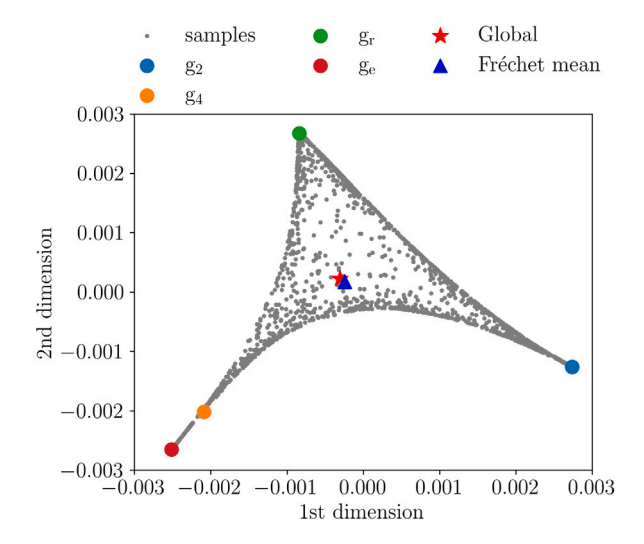


Fig. 7. Visualization of the dataset, given by the four nominal reduced-order bases corresponding to the model candidates, and 2000 additional samples (reduced-order displacement equation). Spectral embedding is used to project data in St(2501,10) onto \mathbb{R}^2 .

4.1.2.2. Sampling of stochastic reduced-order bases. In order to generate realizations of the stochastic reduced-order basis, the concentration parameters are first calculated by solving the quadratic programming problem defined in Eq. (44). It is found that $\alpha = (0.347, 0.273, 0.184, 0.195)^T$. The first three modes of 100 generated basis samples are shown in Fig. 6. It is seen that all realizations are quite uniformly distributed within the domain defined by the modes of the four nominal reduced-order bases, and that the zero boundary condition is also satisfied on the left end of the bar. In order to observe the localization of the samples without restricting attention to particular modes, the spectral embedding approach developed in [23] can be used to project samples from St(2501, 10) onto the two-dimensional Euclidean space; see Fig. 7. It is observed that the generated samples are located within the convex hull defined by the nominal reduced-order bases (i.e., $[\Phi_u^{(1)}]$, $[\Phi_u^{(2)}]$, $[\Phi_u^{(3)}]$, and $[\Phi_u^{(4)}]$), due to the Riemannian convex combination. In addition, the Fréchet mean computed over all samples is close to the global reduced-order basis $[\underline{\Phi}_u]$, indicating that the constraint on the mean (see Eq. (42)) is properly satisfied.

4.1.2.3. Propagation of model-form uncertainties. Here, the Monte Carlo approach is used to propagate the model-form uncertainties raised by the selection of the degradation function. Recall that throughout Section 4.1.2, stochastic reduced-order modeling is performed on the displacement equation, and the phase-field equation is solved in full-order. The degradation function corresponding with the random reduced-order basis is selected following the convex combination defined in Eq. (41). A total number of 200 reduced-order basis samples are selected, and the corresponding loading curves are shown in Fig. 8. The 95% confidence intervals, calculated using these loading curves, are shown in Fig. 9. It is seen that all loading curve samples are localized around the loading curves corresponding to the model proposals. It is worth stressing that while the samples of the stochastic reduced-order basis belong to the convex hull defined by the nominal reduced-order bases, there is no mathematical results related to the localization of samples once propagated through the reduced-order model (due to nonlinearities). Stronger concentration is observed around nominal curves (in colored lines), in accordance with the concentration of samples in Fig. 7. These first results demonstrate the capability of the proposed framework to encode model-form uncertainties in phase-field simulations. In the next section, we assess the performance of the technique considering the reduced-order phase-field equation.

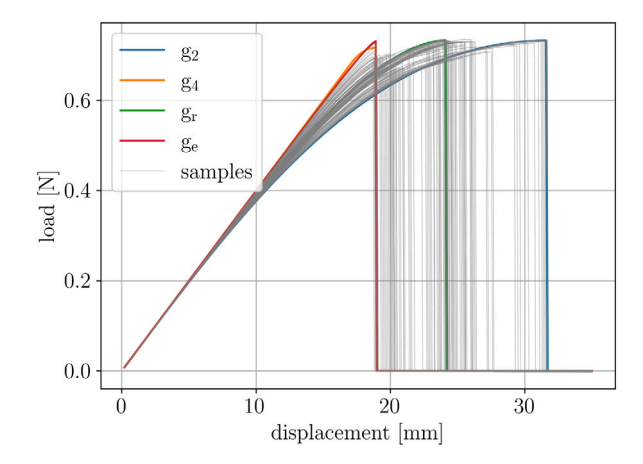


Fig. 8. Loading curves associated with 200 samples of the stochastic reduced-order basis, computed with the Monte Carlo approach (reduced-order displacement equation).

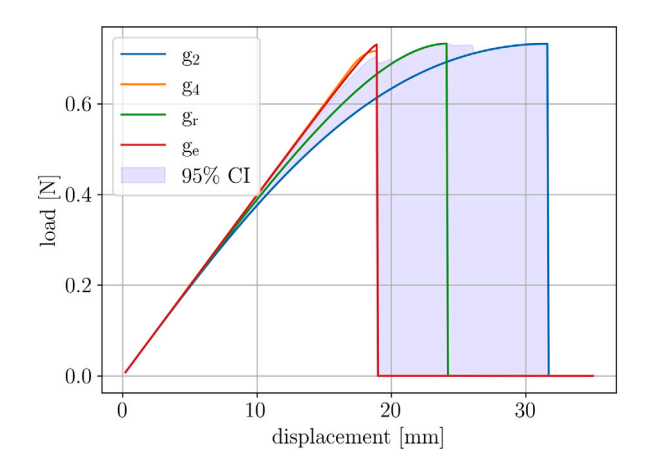


Fig. 9. The 95% confidence interval of the loading curve samples (reduced-order displacement equation).

4.1.3. Stochastic simulations with reduced-order phase-field equation

In this section, the stochastic reduced-order modeling approach is deployed on the phase-field equation (see Section 3.1.2).

4.1.3.1. Computation of the nominal reduced-order bases. The graph of the error function $r \mapsto \epsilon(r)$ for all nominal models is shown in Fig. 10. In this setup, the error threshold $\overline{\epsilon}$ is chosen as 10^{-5} , and 15 modes (n=15) are finally selected to build the reduced-order bases $[\Phi_d^{(1)}]$, $[\Phi_d^{(2)}]$, $[\Phi_d^{(3)}]$, $[\Phi_d^{(4)}]$, and $[\underline{\Phi}_d]$. This choice leads to stochastic modeling of reduced-order bases in $\mathbb{S}_{2501,15} \subset St(2501,15)$ (as opposed to $\mathbb{S}_{2501,10} \subset St(2501,10)$ for the displacement equation).

4.1.3.2. Sampling of stochastic reduced-order bases. Here, the concentration parameters are found to be $\alpha = (0.343, 0.192, 0.178, 0.287)^T$. The first three modes of the initial reduced-order bases, together with 100 additional realizations of the modes, are shown in Fig. 11. As with the reduced-order displacement equation, it is seen that the samples are located within the domain defined by the four nominal reduced-order bases. It is also worth mentioning that all the generated reduced-order bases have fixed zero boundary values on the two ends, illustrating again that the linear constraint $[B_d]^T[\Phi] = [0_{N_{CD},n}]$ (see Eq. (30)) is satisfied through the use of the Riemannian operators (almost surely). It is seen that the samples are properly located within the convex hull defined by $[\Phi_d^{(1)}]$, $[\Phi_d^{(3)}]$, $[\Phi_d^{(3)}]$, $[\Phi_d^{(3)}]$, $[\Phi_d^{(3)}]$, $[\Phi_d^{(3)}]$, $[\Phi_d^{(3)}]$, and $[\Phi_d^{(4)}]$. It is also observed that the Fréchet mean of the generated samples is fairly close to $[\underline{\Phi}_d]$, demonstrating once again the relevance of the procedure given at the end of Section 3.2.

Fig. 12 shows the localization of (projected) samples in \mathbb{R}^2 , using spectral embedding.

4.1.3.3. Propagation of model-form uncertainties. Loading curves corresponding to the nominal reduced-order bases and additional samples are shown in Fig. 13. The corresponding 95% confidence intervals are shown in Fig. 14. The results obtained for the reduced-order phase-field equation are similar to those obtained with the reduced-order displacement equation: the spread generated by the different degradation functions g_2 , g_4 , g_r , and g_e , is well captured.

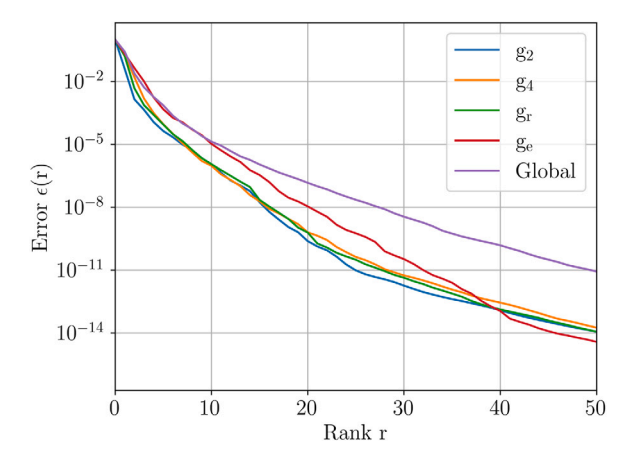


Fig. 10. Graph of the error function $r \mapsto \epsilon(r)$ (see Eq. (24)) for all models (reduced-order phase-field equation). Recall that the global reduced-order basis is obtained by merging all solution snapshots for all models.

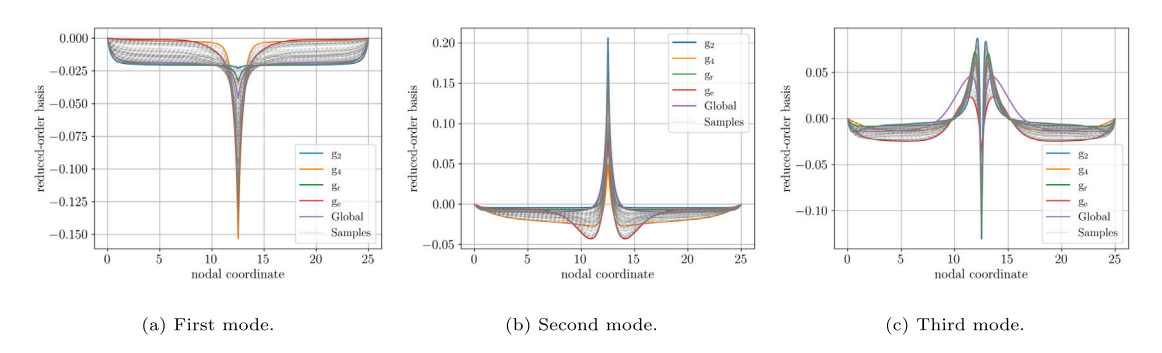


Fig. 11. First three modes of the initial reduced-order bases $[\Phi_d^1]$, $[\Phi_d^2]$, $[\Phi_d^2]$, $[\Phi_d^4]$ (colored lines), and 100 additional samples (reduced-order phase-field equation). (For interpretation of the references to color in this figure legend, the reader is referred to the web version of this article.)

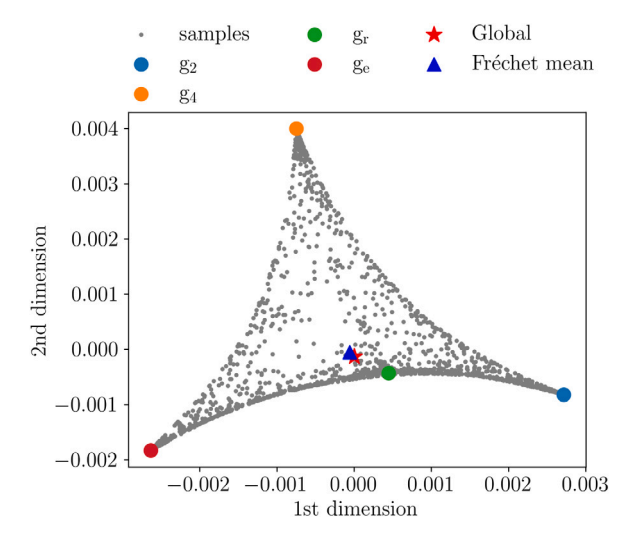


Fig. 12. Visualization of the dataset, given by the four nominal reduced-order bases corresponding to the model candidates, and 2000 additional samples (reduced-order phase-field equation). Spectral embedding is used to project data in St(2501,10) onto \mathbb{R}^2 .

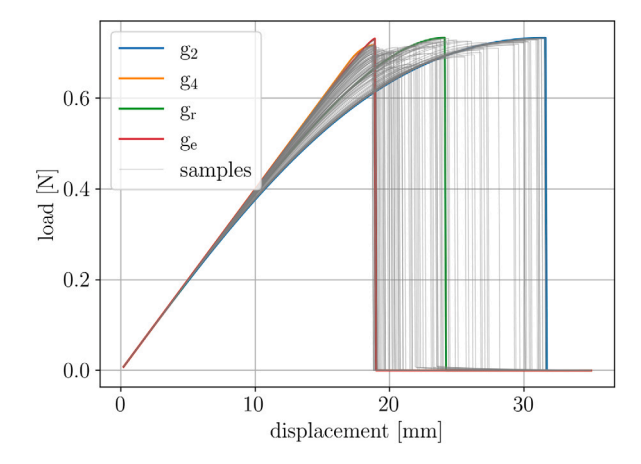


Fig. 13. Loading curves associated with 200 samples of the stochastic reduced-order basis, computed with the Monte Carlo approach (reduced-order phase-field equation).

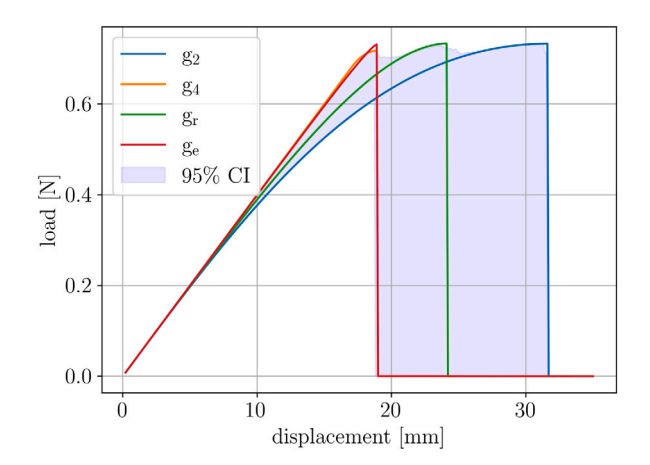


Fig. 14. The 95% confidence interval of the loading curve samples (reduced-order phase-field equation).

4.2. Two-dimensional tensile test

4.2.1. Problem description

We now consider a two-dimensional domain, subjected to a tensile test; see Fig. 15. The bottom boundary is fixed, while a vertical displacement \bar{u} is applied on the top boundary. The maximum displacement is 0.065 [mm] and is applied through increments of 0.001 [mm]. The bulk modulus is set to 121.154 [GPa], shear modulus is 80.769 [GPa], and the fracture energy G_c is taken as 2.7×10^3 [J m⁻²]. Regarding the finite element discretization, linear triangular elements are employed, with a minimum characteristic size of 0.004 [mm] near the fractured region (based on a mesh convergence analysis). The mesh contains 16,904 nodes. Recall that the hybrid scheme proposed in [21] is used to accelerate computations.

The degradation functions $\{g_2, g_3, g_r, g_e\}$ are employed in the phase-field fracture simulations. In order to match the peak load obtained from different degradation functions, the regularization length ℓ is set to $\{0.02, 0.03, 0.02, 0.016\}$ [mm] for the four selected models, respectively. The initial and final damage fields obtained with the quadratic degradation function are shown in Fig. 16. The four loading curves corresponding with the above degradation functions are shown in Fig. 17. In this case, the choice of the degradation function does not generate large variability in the mechanical response, which allows us to test the framework in the asymptotic regime where statistical fluctuations tend to zero.

4.2.2. Sampling of stochastic reduced-order bases

The stochastic modeling and sampling tasks are separately carried out for the reduced-order displacement and phase-field equations. The reduced-order bases $\{[\boldsymbol{\Phi}_u^{(1)}], [\boldsymbol{\Phi}_u^{(2)}], [\boldsymbol{\Phi}_u^{(3)}], [\boldsymbol{\Phi}_u^{(4)}]\}$, and the global reduced-order basis $[\underline{\boldsymbol{\Phi}}_u]$ are first calculated for the displacement equation. Similarly, we calculate the reduced-order basis $\{[\boldsymbol{\Phi}_d^{(1)}], [\boldsymbol{\Phi}_d^{(2)}], [\boldsymbol{\Phi}_d^{(3)}], [\boldsymbol{\Phi}_d^{(4)}]\}$, together with the global reduced-order basis $[\underline{\boldsymbol{\Phi}}_d]$ for the phase-field equation. In order to determine the truncation modes of the reduced-order basis, the truncation error functions are computed following Eq. (24), and are shown in Fig. 18. With the threshold set to 10^{-5} , the nominal reduced-order

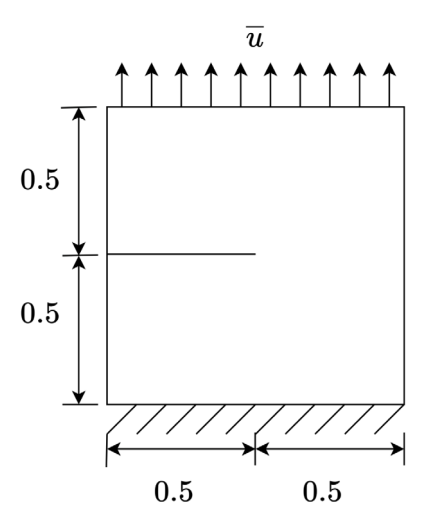


Fig. 15. The computational domain of phase-field simulation of tensile case with a single notch in the middle.

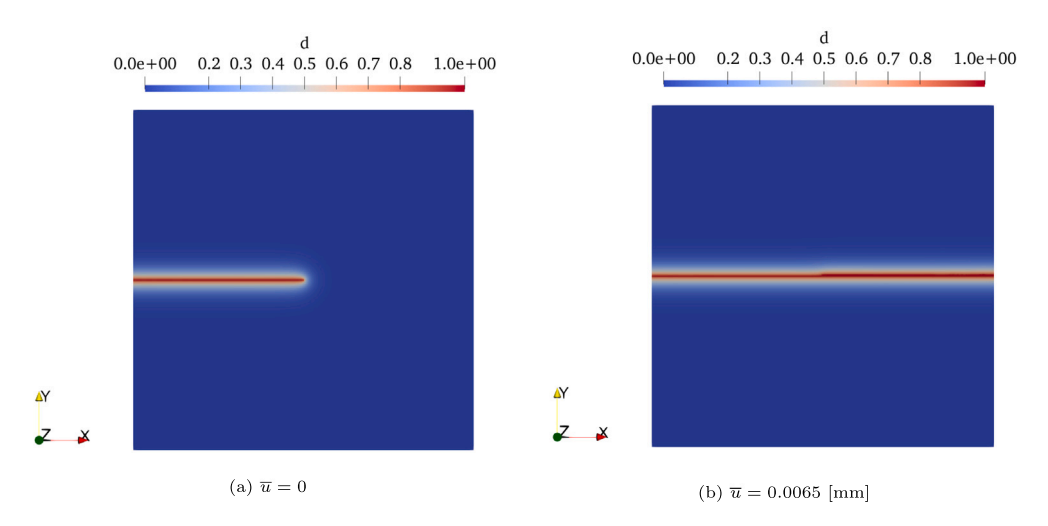


Fig. 16. Initial damage field (left) and final damage field obtained for $\bar{u} = 0.0065$ [mm] (right).

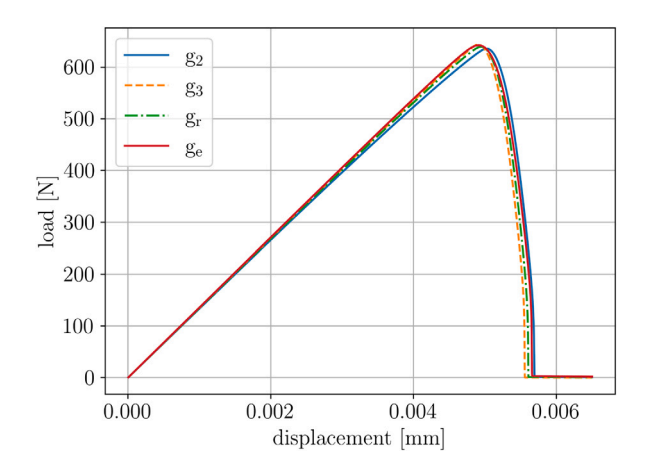


Fig. 17. Loading curves simulated for all model candidates, with $\ell \in \{0.02, 0.03, 0.02, 0.016\}$ [mm].

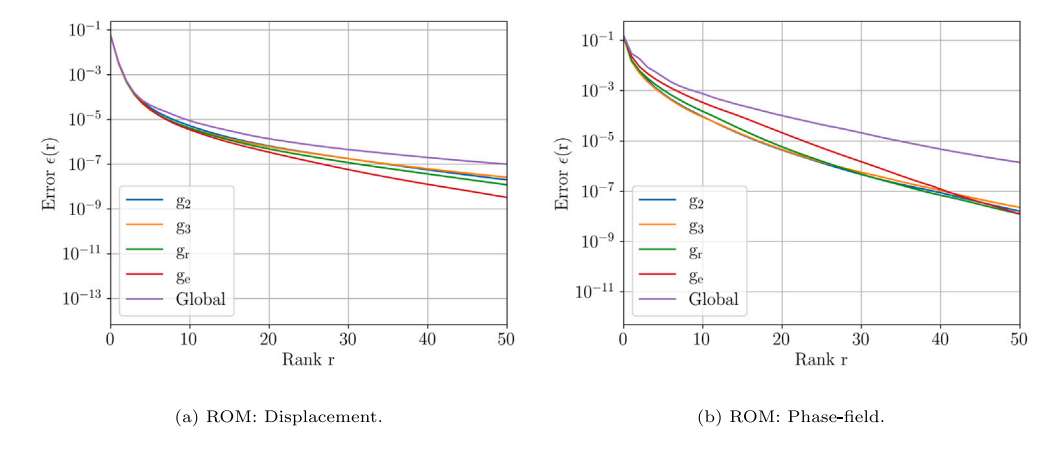


Fig. 18. Graph of the error function $r \mapsto \epsilon(r)$ for all models and the two scenarios. Recall that the global reduced-order basis is obtained by merging all solution snapshots for all models.

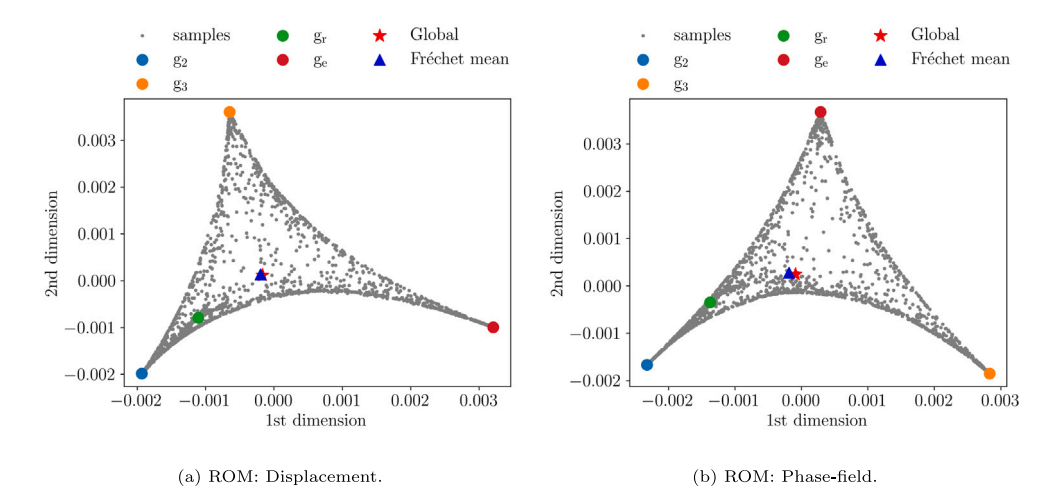


Fig. 19. Visualization of the dataset, given by the four nominal reduced-order bases corresponding to the model candidates, and 2000 additional samples (reduced-order displacement and phase-field equations).

bases are finally obtained by retaining the first 30 modes of the eigenvectors. Therefore, the stochastic reduced-order bases $[\boldsymbol{\Phi}_d]$ will be sampled in the space $\mathbb{S}_{16904,30} \subset St(16904,30)$, while $[\boldsymbol{\Phi}_u]$ will be sampled in space $\mathbb{S}_{33808,30} \subset St(33808,30)$.

In order to generate samples of the stochastic reduced-order bases $[\boldsymbol{\Phi}_d]$ and $[\boldsymbol{\Phi}_u]$, the concentration parameters must be determined by solving the quadratic programming problem given by Eq. (44). The vector of hyperparameters defining the Dirichlet distribution was found to be $\boldsymbol{\alpha} = (0.323, 0.350, 0.104, 0.223)^T$ for $[\boldsymbol{\Phi}_d]$, and $\boldsymbol{\alpha} = (0.314, 0.236, 0.099, 0.351)^T$ for $[\boldsymbol{\Phi}_u]$. Additional samples are shown in Fig. 19, using the spectral embedding technique. It can be seen that all the generated samples are within the (projected) convex hull of the original five original reduced-order bases, and the global reduced order basis is close to the Fréchet mean of the samples, indicating that the constraint on the model mean (see Eq. (42)) is satisfied.

4.2.3. Propagation of model-form uncertainties

Monte Carlo simulations are conducted to propagate and quantify the model-form uncertainties by solving the reduced-order phase-field or displacement equation. Samples of the computed loading curves are shown in Fig. 20 for each scenario. The corresponding 95% confidence intervals are further shown in Fig. 21. It can be seen that the generated loading curve samples cover the domain of the original four loading curves, for each scenario. It is also observed that some samples are located outside the domain defined by the nominal loading curves, especially for the reduced-order phase-field problem. As previously indicated, there is no mathematical result ensuring concentration at the propagation stage. In the case where such fluctuations must be contained, the strategy to calibrate the hyperparameters must be adapted accordingly, by formulating an inverse problem involving confidence intervals for instance. This aspect is outside the scope of this work and is left for future work.

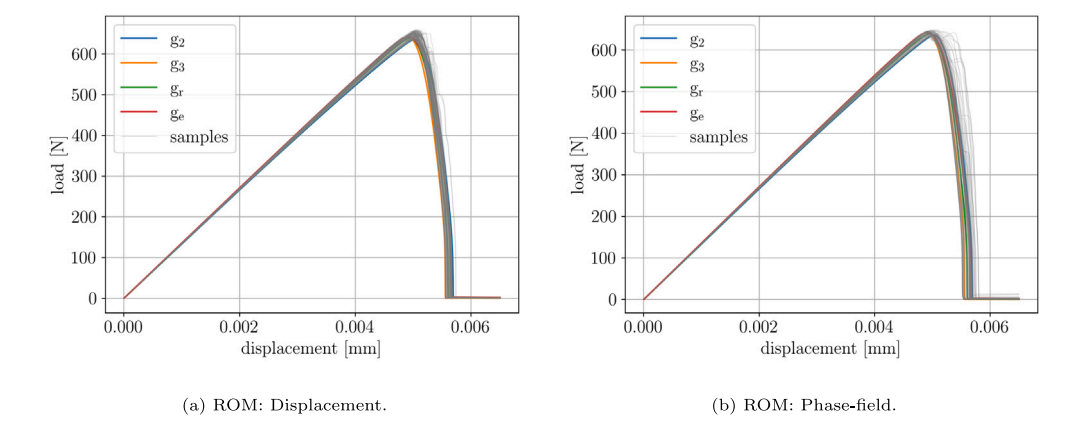


Fig. 20. 200 samples of the loading curve estimated with the stochastic reduced-order displacement (left) and phase-field (right) equation.

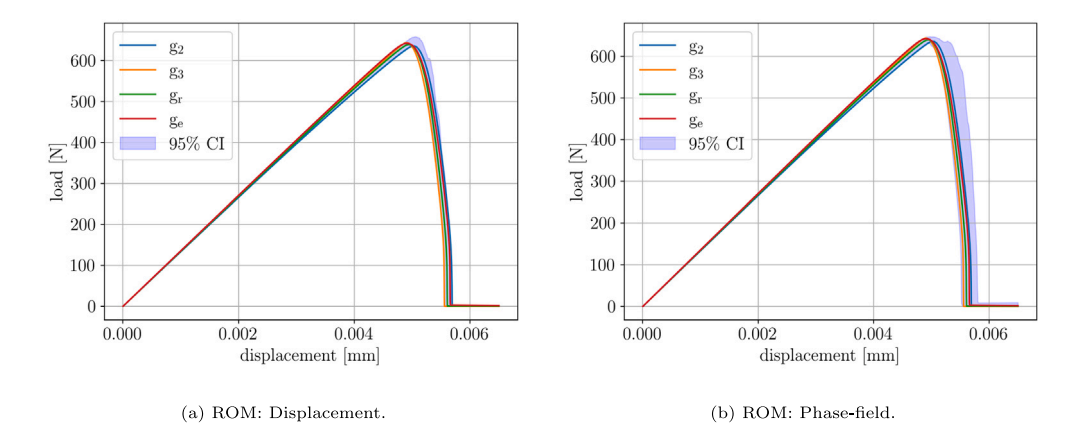


Fig. 21. 95% confidence interval of the loading curve estimated with the stochastic reduced-order displacement (left) and phase-field (right) equation.

4.3. Two-dimensional shear test

4.3.1. Problem description

In this section, stochastic phase-field fracture simulations are conducted on a two-dimensional domain undergoing a shear load. An initial notch is located in the middle of the domain, as shown in Fig. 22. The size of the square is 1×1 [mm]. Linear triangular finite elements are used with a characteristic size of 0.004 [mm] near the fracture path, leading to a total number of 21,085 nodes. During the simulation, the bottom boundary is fixed and a Dirichlet boundary condition is applied on the top boundary, with increments of 1×10^{-5} [mm] (maximal displacement is set to 0.025 [mm]). The spectral decomposition split is used in the simulations. Material parameters coincide with those used in the tensile test (see Section 4.2.1).

Three degradation functions, namely $\{g_2, g_3, g_r\}$, are selected to introduce model uncertainties. We use the same length scales as those determined in the tensile test (i.e., 0.02, 0.03, and 0.02 [mm]), noticing that they also yield close maximum peak loads (see Fig. 24). The damage field corresponding to the degradation function g_2 can be seen in Fig. 23 at the initial stage and final (fully-broken) stage, respectively. Note that results for the other degradation functions are not shown since the fracture paths are visually close to one another. The loading curves are shown in Fig. 24.

In contrast with the tensile test, the choice of the degradation function generates stronger variability, particularly in the softening regime.

4.3.2. Sampling of stochastic reduced-order bases

The truncation error functions for the reduced-order displacement and phase-field problems are shown in Fig. 25. With a threshold set to 10^{-5} , 30 modes are selected for both problems. The concentration parameters are obtained as $\alpha = (0.337, 0.401, 0.262)^T$ for $[\boldsymbol{\Phi}_u]$, and $\alpha = (0.374, 0.441, 0.185)^T$ for $[\boldsymbol{\Phi}_d]$. Samples generated with these hyperparameters are shown in Fig. 26.

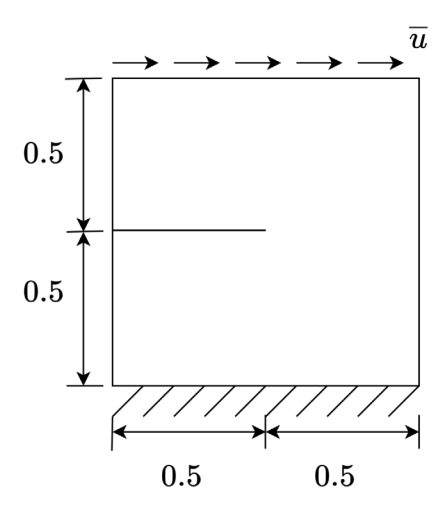


Fig. 22. Computational domain and boundary conditions.

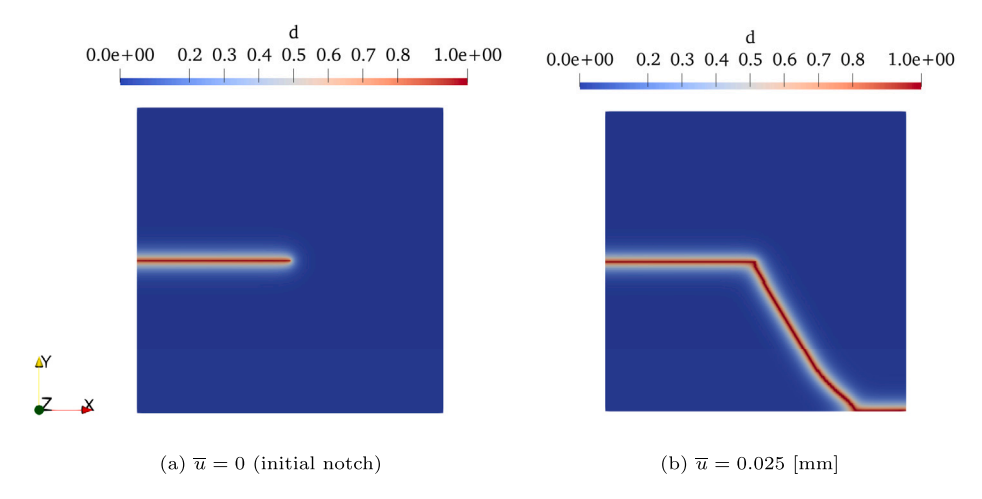


Fig. 23. Initial notch (left) and fracture path (right) at $\bar{u} = 0.025$ [mm].

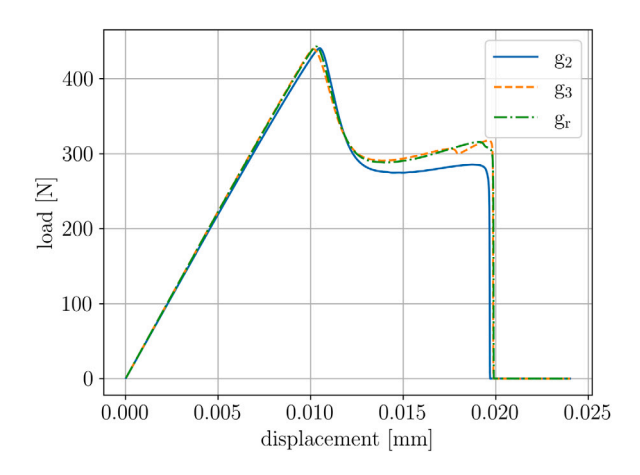


Fig. 24. Loading curves simulated for all model candidates, with $\ell \in \{0.02, 0.03, 0.02\}$ [mm].

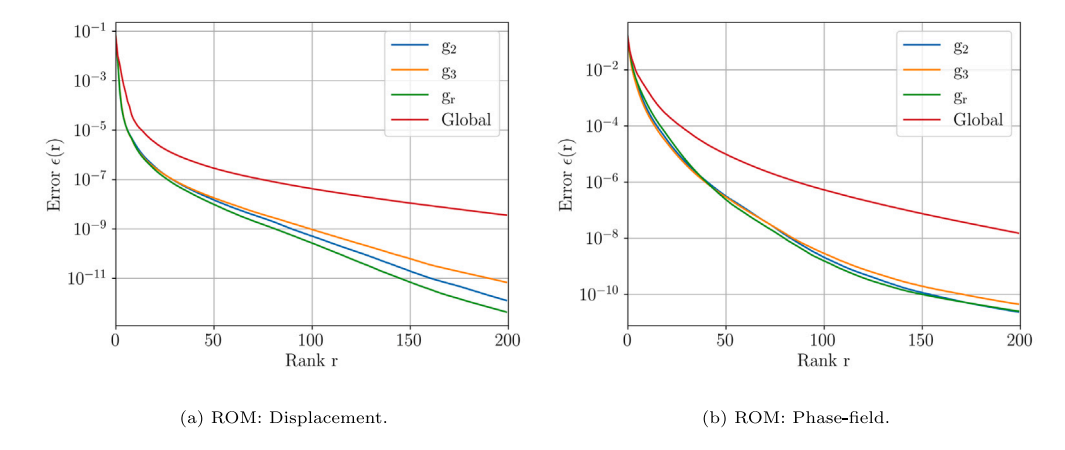


Fig. 25. Graph of the error function $r \mapsto \epsilon(r)$ for all models and the two scenarios. Recall that the global reduced-order basis is obtained by merging all solution snapshots for all models.

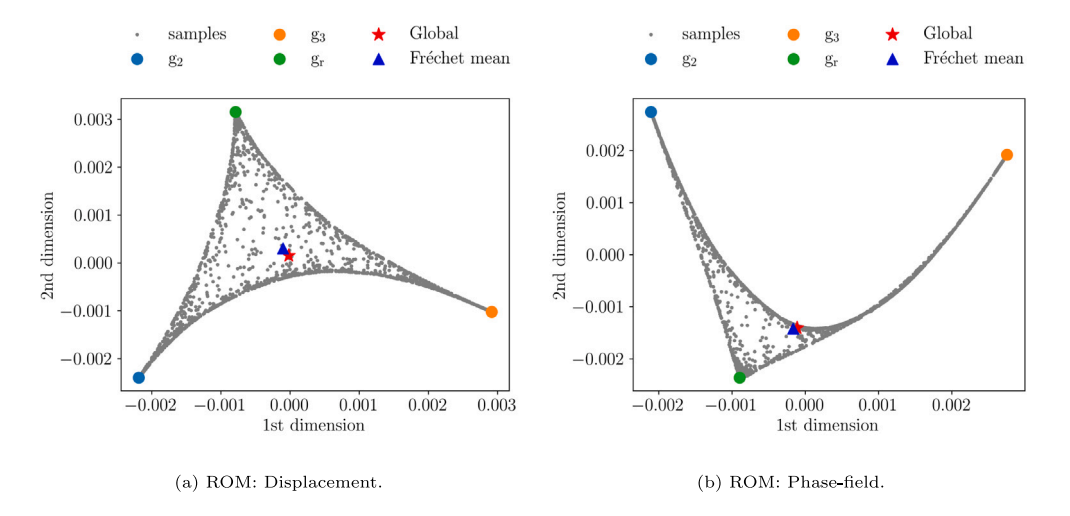


Fig. 26. Low-dimensional representation of the reduced-order basis samples. Spectral embedding approach is used to perform dimension reduction.

4.3.3. Propagation of model-form uncertainties

Model-form uncertainties are propagated through direct Monte Carlo simulations. Fig. 27 shows the 95% confidence intervals estimated with 200 loading curve samples. It is seen that most of the loading curve samples are distributed beyond the domain defined by nominal responses, with a very noticeable trend observed for the reduced-order displacement problem. From a quantitative standpoint, approximately 84% of the loading curves fail to match the peak stress with the reduced-order displacement simulation, while 62% loading curves fail to capture the fully cracked region with the reduced-order phase-field simulation. A plausible explanation lies in the sensitivity of the forward simulations in shear, where samples of the reduced-order basis can generate nonphysical oscillations in the damage field away from the crack path—which may, in turn, generate larger discrepancies in the loading curves. This observation is illustrated in Figs. 28 and 29, where snapshots of the damage field at various loading stages, obtained with the reduced-order models, are shown. A remedy to circumvent this issue through selected randomization in discussed in the following section.

4.3.4. Stabilization through localized randomization

One possible strategy to stabilize the response near an average forward operator is to introduce a block matrix decomposition of the reduced-order basis where (i) low-frequency modes are kept deterministic and define the mean response around which perturbations are prescribed, and (ii) high-frequency modes are randomized following the procedure in Section 3.2 to generate localized fluctuations. For a given reduced-order formulation (in displacement or in the phase-field variable), recall that $[\underline{\Phi}]$ denotes the global reduced-order basis, and introduce the block decomposition

$$[\underline{\boldsymbol{\phi}}] = [[\underline{\boldsymbol{\phi}}_{LF}][\underline{\boldsymbol{\phi}}_{HF}][\underline{\boldsymbol{\phi}}_{C}]], \tag{47}$$

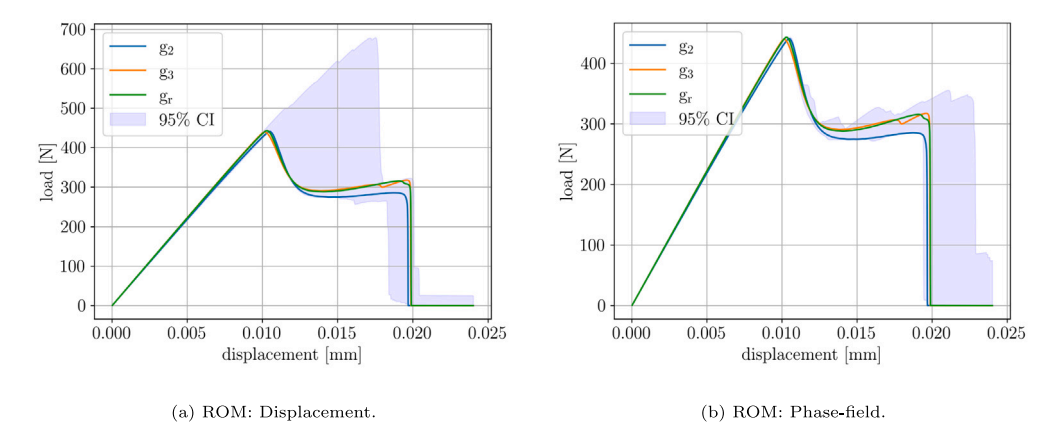


Fig. 27. 95% confidence interval of the loading curve estimated with the stochastic reduced-order displacement (left) and phase-field (right) equation.

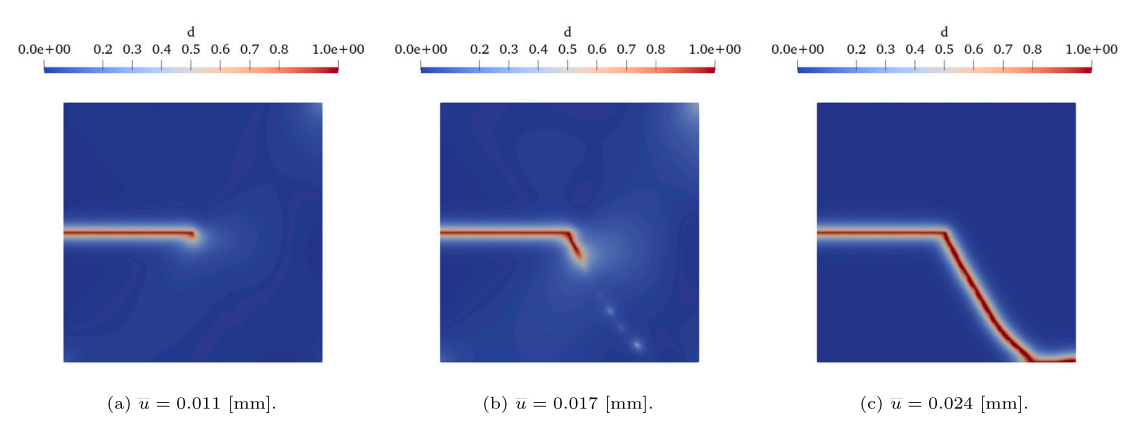


Fig. 28. Damage field predicted with the reduced-order displacement equation, at various loading stages.

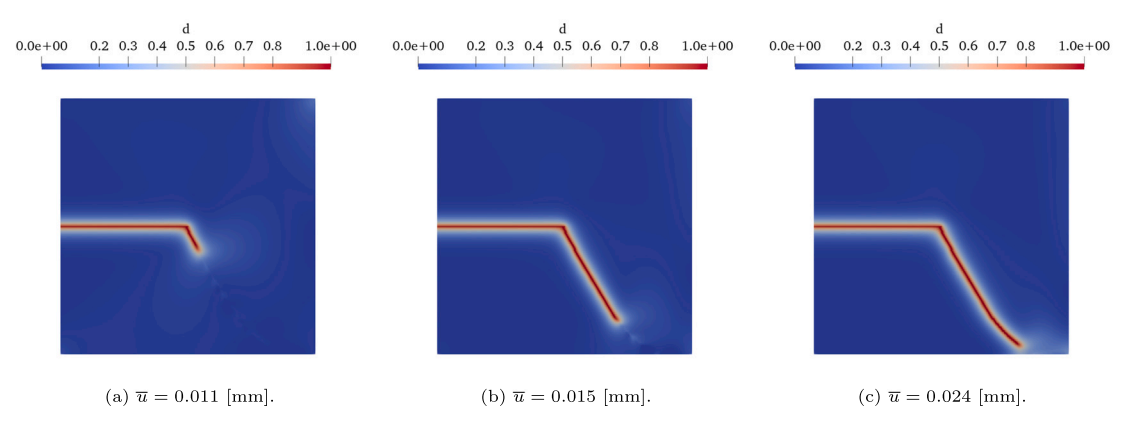


Fig. 29. Damage field predicted with the reduced-order phase-field equation, at various loading stages.

where $[\underline{\Phi}_{LF}] \in \mathbb{R}^{N' \times n_{LF}}$, $[\underline{\Phi}_{HF}] \in \mathbb{R}^{N' \times n_{HF}}$, $[\underline{\Phi}_{C}] \in \mathbb{R}^{N' \times (n-n_{LF}-n_{HF})}$, and $n_{LF}+n_{HF} \leq n$ (in practice, n_{LF} and n_{HF} are chosen such that $n_{LF}+n_{HF} \ll n$). A stabilized formulation can then be obtained by defining the stochastic reduced-order basis as

$$[\boldsymbol{\Phi}_s] = \text{Orth}([[\boldsymbol{\Phi}_{LF}][\boldsymbol{\Phi}_{HF}]]),$$
 (48)

where Orth denotes the Gram-Schmidt orthonormalization operator and $[{m \Phi}_{HF}]$ is defined as

$$[\boldsymbol{\Phi}_{HF}] = \exp_{[\underline{\boldsymbol{\Phi}}_{HF}]}^{St} \left\{ \sum_{i=1}^{m} P_i \log_{[\underline{\boldsymbol{\Phi}}_{HF}]}^{St} ([\boldsymbol{\Phi}_{HF}^{(i)}]) \right\}, \quad \boldsymbol{P} \sim \mathcal{D}(\alpha_1, \dots, \alpha_m),$$

$$(49)$$

where $[\Phi_{HF}^{(i)}]$ is the $(N' \times n_{HF})$ matrix appearing in the following block decomposition of the nominal reduced-order basis $[\Phi^{(i)}]$, associated with the *i*th degradation function (see Section 3.2):

$$[\boldsymbol{\Phi}^{(i)}] = [[\boldsymbol{\Phi}_{LE}^{(i)}][\boldsymbol{\Phi}_{HE}^{(i)}][\boldsymbol{\Phi}_{C}^{(i)}]], \tag{50}$$

with $[\boldsymbol{\Phi}_{LF}^{(i)}] \in \mathbb{R}^{N' \times n_{LF}}$, $[\boldsymbol{\Phi}_{HF}^{(i)}] \in \mathbb{R}^{N' \times n_{HF}}$, and $[\boldsymbol{\Phi}_{C}^{(i)}] \in \mathbb{R}^{N' \times (n-n_{LF}-n_{HF})}$. Here, the concentration parameters $\boldsymbol{\alpha} = (\alpha_1, \dots, \alpha_m)^T$ are calibrated by using the procedure defined in Section 3.2, with

$$\mathbb{E}\{[\boldsymbol{\phi}_{HF}]\} \approx [\underline{\boldsymbol{\phi}}_{HF}]. \tag{51}$$

By construction, the stochastic reduced-order basis $[\Phi_s]$ defined by Eq. (48) belongs to the Stiefel manifold St(N', n) almost surely. To ensure admissibility, we now establish the following

Proposition 1. The stochastic reduced-order basis $[\Phi_s]$ defined by Eq. (48) satisfies the linear constraint

$$[B]^T [\boldsymbol{\Phi}_s] = [0_{N_{CD} \times n}] \tag{52}$$

almost surely.

Proof. Let $[\underline{\boldsymbol{\Phi}}_{LF}] = [\boldsymbol{v}^{(1)}, \dots, \boldsymbol{v}^{(n_{LF})}]$ and $[\boldsymbol{\Phi}_{HF}] = [\boldsymbol{V}^{(n_{LF}+1)}, \dots, \boldsymbol{V}^{(n_{LF}+n_{HF})}]$ (recall that vectors in $[\underline{\boldsymbol{\Phi}}_{LF}]$ and $[\boldsymbol{\Phi}_{HF}]$ are deterministic and random, respectively). By construction, $[B]^T \boldsymbol{v}^{(j)} = \boldsymbol{0}_{N_{CD}}$ for $1 \leq j \leq n_{LF}$, and $[B]^T \boldsymbol{V}^{(j)} = \boldsymbol{0}_{N_{CD}}$ almost surely for $n_{LF} + 1 \leq j \leq n_{LF}$, $[D]^T \boldsymbol{U}^{(j)} = \boldsymbol{0}_{N_{CD}}$ for $1 \leq j \leq n_{LF}$ almost surely. Hence, $[B]^T \boldsymbol{U}^{(j)} = \boldsymbol{0}_{N_{CD}}$ for $1 \leq j \leq n_{LF}$ almost surely. Next, apply the Gram–Schmidt procedure to get

$$\boldsymbol{U}^{(n_{LF}+1)} = \frac{\boldsymbol{W}^{(n_{LF}+1)}}{\|\boldsymbol{W}^{(n_{LF}+1)}\|}, \quad \boldsymbol{W}^{(n_{LF}+1)} = \boldsymbol{V}^{(n_{LF}+1)} - \sum_{j=1}^{n_{LF}} \boldsymbol{U}^{(j)},$$
(53)

which shows that $[B]^T U^{(n_{LF}+1)} = \mathbf{0}_{N_{CD}}$ almost surely. Proceeding along iterations

$$\boldsymbol{U}^{(k+1)} = \frac{\boldsymbol{W}^{(k+1)}}{\|\boldsymbol{W}^{(k+1)}\|}, \quad \boldsymbol{W}^{(k+1)} = \boldsymbol{V}^{(k+1)} - \sum_{j=1}^{n_{LF}} \boldsymbol{U}^{(j)} - \sum_{j=n_{LF}+1}^{k} \frac{\langle \boldsymbol{V}^{(j)}, \boldsymbol{W}^{(j)} \rangle}{\langle \boldsymbol{W}^{(j)}, \boldsymbol{W}^{(j)} \rangle} \boldsymbol{W}^{(j)}, \quad \forall k \ge n_{LF} + 1,$$
(54)

and using the above results completes the proof. \Box

In practice, the number of low-frequency modes n_{LF} is chosen to capture the peak stress with the reduced-order model (either in displacement or in the phase-field variable) involving the global ROB, while the number of stochastic high-frequency modes n_{HF} is set of induce a desired level of fluctuations.

Results obtained with the above procedure and for the two types of reduced-order models are provided below. For the displacement ROM, 50 low-frequency eigenmodes are retained, while 40 low-frequency eigenmodes are used for the phase-field ROM. In both cases, 30 high-frequency eigenmodes are randomized to induce statistical fluctuations. Fig. 30 shows the distribution of 1000 samples. Fig. 31 shows 95% confidence intervals for the loading curves.

As expected, these results demonstrate better stability in the forward propagation problem.

5. Conclusion

A stochastic modeling framework enabling the representation of model-form uncertainties in brittle fracture simulations was presented. Leveraging recent results derived in the context of nonlinear dynamical analysis, the proposed approach relies on the construction of a stochastic reduced-order model, the projection basis of which is randomized using Riemannian projection and retraction operators, as well as an information-theoretic formulation. The model thus obtained, applied in a phase-field setting, ensures mathematical consistency in terms of orthogonality and satisfaction of boundary conditions. The proposed formulation involves a low-dimensional parameterization, which can be readily calibrated solving a quadratic programming problem, and is easy to implement.

The relevance of the modeling approach was assessed on one- and two-dimensional applications. It was shown that model uncertainties can be properly encoded and efficiently propagated to macroscopic quantities of interest (here, the loading curve). An extension based on localized randomization was finally proposed to handle the case where the forward simulation is highly sensitive to sample localization.

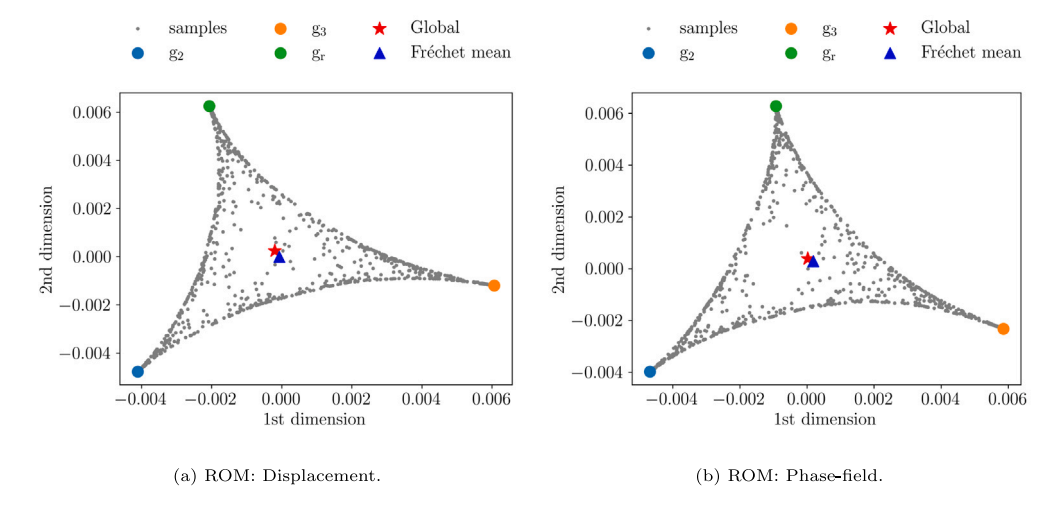


Fig. 30. Low-dimensional representation of the reduced-order basis samples. Spectral embedding approach is used to perform dimension reduction.

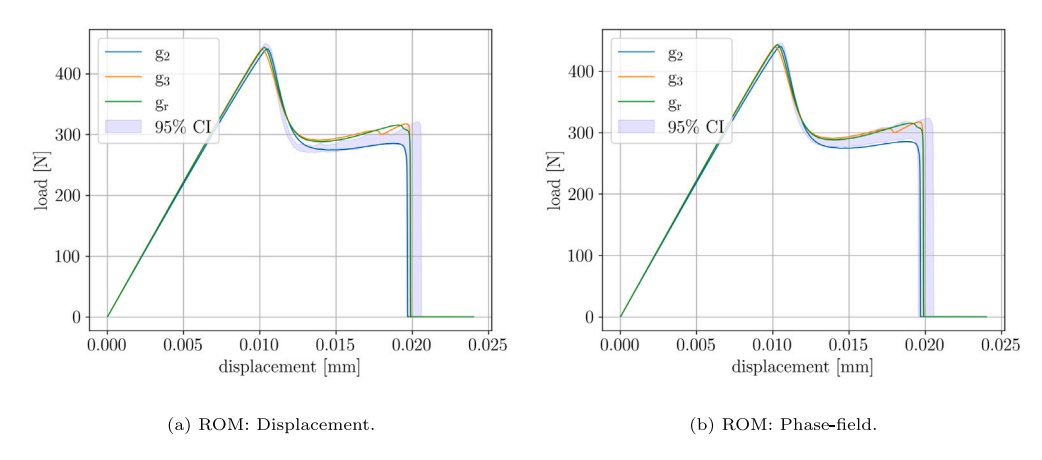


Fig. 31. 95% confidence interval of the loading curve estimated with the stochastic reduced-order displacement (left) and phase-field (right) equation, using the stabilized formulation.

This work constitutes a methodological development allowing phase-field predictions to be endowed with statistical measures of confidence, accounting for the variability induced by modeling choices. While the framework was demonstrated on simple canonical problems, it remains applicable to more complex fracture scenarios, due to its formulation in the reduced-order space. The consideration of more challenging settings (involving, e.g., multi-axial loading) is expected to impact reducibility and discretization, which may in turn increase the computational cost associated with the projection and retraction operations. Extensions to alleviate these issues, together with the consideration of alternative reduction techniques (for almost irreducible systems), are left for future work.

Declaration of competing interest

The authors declare the following financial interests/personal relationships which may be considered as potential competing interests: Johann Guilleminot reports financial support was provided by National Science Foundation. Johann Guilleminot reports financial support was provided by US Army Research Laboratory.

Data availability

Data will be made available on request.

Acknowledgments

The work of H. Z. and J. G. was supported by the National Science Foundation, Division of Civil, Mechanical and Manufacturing Innovation, under award CMMI-1942928, and by the Army Research Office, USA under grant W911NF-23-1-0125. The authors would like to thank Dr. Rudy Geelen for useful discussions regarding the implementation of the phase-field method in FEniCS.

References

- [1] G.A. Francfort, J.-J. Marigo, Revisiting brittle fracture as an energy minimization problem, J. Mech. Phys. Solids 46 (8) (1998) 1319–1342, http://dx.doi.org/10.1016/S0022-5096(98)00034-9.
- [2] B. Bourdin, G.A. Francfort, J.-J. Marigo, Numerical experiments in revisited brittle fracture, J. Mech. Phys. Solids 48 (4) (2000) 797-826.
- [3] B. Carter, P. Wawrzynek, A. Ingraffea, Automated 3-D crack growth simulation, Internat. J. Numer. Methods Engrg. 47 (1–3) (2000) 229–253, http://dx.doi.org/10.1002/(SICI)1097-0207(20000110/30)47:1/3%3C229::AID-NME769%3E3.0.CO;2-2.
- [4] N. Sukumar, J. Dolbow, N. Moës, Extended finite element method in computational fracture mechanics: A retrospective examination, Int. J. Fract. 196 (2015) 189–206, http://dx.doi.org/10.1007/s10704-015-0064-8.
- [5] B. Bourdin, G.A. Francfort, J.-J. Marigo, The variational approach to fracture, J. Elasticity 91 (2008) 5-148, http://dx.doi.org/10.1007/s10659-007-9107-3.
- [6] C. Kuhn, R. Müller, A continuum phase field model for fracture, Eng. Fract. Mech. 77 (18) (2010) 3625–3634, http://dx.doi.org/10.1016/j.engfracmech. 2010.08.009.
- [7] T.Q. Bui, X. Hu, A review of phase-field models, fundamentals and their applications to composite laminates, Eng. Fract. Mech. 248 (2021) 107705, http://dx.doi.org/10.1016/j.engfracmech.2021.107705.
- [8] C. Wu, J. Fang, Z. Zhang, A. Entezari, G. Sun, M.V. Swain, Q. Li, Fracture modeling of brittle biomaterials by the phase-field method, Eng. Fract. Mech. 224 (2020) 106752, http://dx.doi.org/10.1016/j.engfracmech.2019.106752.
- [9] Y. Heider, A review on phase-field modeling of hydraulic fracturing, Eng. Fract. Mech. 253 (2021) 107881, http://dx.doi.org/10.1016/j.engfracmech.2021. 107881
- [10] M. Ambati, T. Gerasimov, L. De Lorenzis, Phase-field modeling of ductile fracture, Comput. Mech. 55 (2015) 1017–1040, http://dx.doi.org/10.1007/s00466-015-1151-4.
- [11] C. Miehe, F. Aldakheel, A. Raina, Phase field modeling of ductile fracture at finite strains: A variational gradient-extended plasticity-damage theory, Int. J. Plast. 84 (2016) 1–32, http://dx.doi.org/10.1016/j.ijplas.2016.04.011.
- [12] T. Hu, B. Talamini, A.J. Stershic, M.R. Tupek, J.E. Dolbow, A variational phase-field model for ductile fracture with coalescence dissipation, Comput. Mech. 68 (2) (2021) 311–335, http://dx.doi.org/10.1007/s00466-021-02033-1.
- [13] C.V. Verhoosel, R. de Borst, A phase-field model for cohesive fracture, Internat. J. Numer. Methods Engrg. 96 (1) (2013) 43–62, http://dx.doi.org/10. 1002/nme.4553.
- [14] T.-T. Nguyen, J. Yvonnet, Q.-Z. Zhu, M. Bornert, C. Chateau, A phase-field method for computational modeling of interfacial damage interacting with crack propagation in realistic microstructures obtained by microtomography, Comput. Methods Appl. Mech. Engrg. 312 (2016) 567–595, http://dx.doi.org/10.1016/j.cma.2015.10.007.
- [15] P. Zhang, X. Hu, X. Wang, W. Yao, An iteration scheme for phase field model for cohesive fracture and its implementation in Abaqus, Eng. Fract. Mech. 204 (2018) 268–287, http://dx.doi.org/10.1016/j.engfracmech.2018.10.006.
- [16] M. Hofacker, C. Miehe, Continuum phase field modeling of dynamic fracture: Variational principles and staggered FE implementation, Int. J. Fract. 178 (2012) 113–129, http://dx.doi.org/10.1007/s10704-012-9753-8.
- [17] R.J. Geelen, Y. Liu, T. Hu, M.R. Tupek, J.E. Dolbow, A phase-field formulation for dynamic cohesive fracture, Comput. Methods Appl. Mech. Engrg. 348 (2019) 680–711, http://dx.doi.org/10.1016/j.cma.2019.01.026.
- [18] H. Ren, X. Zhuang, C. Anitescu, T. Rabczuk, An explicit phase field method for brittle dynamic fracture, Comput. Struct. 217 (2019) 45–56, http://dx.doi.org/10.1016/j.compstruc.2019.03.005.
- [19] J.-Y. Wu, V.P. Nguyen, C.T. Nguyen, D. Sutula, S. Sinaie, S.P. Bordas, Phase-field modeling of fracture, Adv. Appl. Mech. 53 (2020) 1–183, http://dx.doi.org/10.1016/bs.aams.2019.08.001.
- [20] X. Zhuang, S. Zhou, G. Huynh, P. Areias, T. Rabczuk, Phase field modeling and computer implementation: A review, Eng. Fract. Mech. 262 (2022) 108234, http://dx.doi.org/10.1016/j.engfracmech.2022.108234.
- [21] M. Ambati, T. Gerasimov, L. De Lorenzis, A review on phase-field models of brittle fracture and a new fast hybrid formulation, Comput. Mech. 55 (2015) 383–405, http://dx.doi.org/10.1007/s00466-014-1109-y.
- [22] R. Ghanem, D. Higdon, H. Owhadi, Handbook of Uncertainty Quantification, Vol. 6, Springer, 2017.
- [23] U. Von Luxburg, A tutorial on spectral clustering, Stat. Comput. 17 (4) (2007) 395–416, http://dx.doi.org/10.1007/s11222-007-9033-z.
- [24] M.J. Borden, T.J. Hughes, C.M. Landis, A. Anvari, I.J. Lee, A phase-field formulation for fracture in ductile materials: Finite deformation balance law derivation, plastic degradation, and stress triaxiality effects, Comput. Methods Appl. Mech. Engrg. 312 (2016) 130–166, http://dx.doi.org/10.1016/j.cma. 2016.09.005.
- [25] C. Kuhn, A. Schlüter, R. Müller, On degradation functions in phase field fracture models, Comput. Mater. Sci. 108 (2015) 374–384, http://dx.doi.org/10. 1016/j.commatsci.2015.05.034.
- [26] E. Lorentz, S. Cuvilliez, K. Kazymyrenko, Modelling large crack propagation: From gradient damage to cohesive zone models, Int. J. Fract. 178 (1–2) (2012) 85–95, http://dx.doi.org/10.1007/s10704-012-9746-7.
- [27] J.M. Sargado, E. Keilegavlen, I. Berre, J.M. Nordbotten, High-accuracy phase-field models for brittle fracture based on a new family of degradation functions, J. Mech. Phys. Solids 111 (2018) 458–489, http://dx.doi.org/10.1016/j.jmps.2017.10.015.
- [28] E. Lorentz, A nonlocal damage model for plain concrete consistent with cohesive fracture, Int. J. Fract. 207 (2) (2017) 123–159, http://dx.doi.org/10. 1007/s10704-017-0225-z.
- [29] Z.A. Wilson, M.J. Borden, C.M. Landis, A phase-field model for fracture in piezoelectric ceramics, Int. J. Fract. 183 (2013) 135–153, http://dx.doi.org/10. 1007/s10704-013-9881-9.
- [30] J.-Y. Wu, A unified phase-field theory for the mechanics of damage and quasi-brittle failure, J. Mech. Phys. Solids 103 (2017) 72–99, http://dx.doi.org/10.1016/j.jmps.2017.03.015.
- [31] R. Alessi, J.-J. Marigo, S. Vidoli, Gradient damage models coupled with plasticity: Variational formulation and main properties, Mech. Mater. 80 (2015) 351–367, http://dx.doi.org/10.1016/j.mechmat.2013.12.005.
- [32] A. Karma, D.A. Kessler, H. Levine, Phase-field model of mode III dynamic fracture, Phys. Rev. Lett. 87 (4) (2001) 045501, http://dx.doi.org/10.1103/ PhysRevLett.87.045501.
- [33] T. Hu, J. Guilleminot, J.E. Dolbow, A phase-field model of fracture with frictionless contact and random fracture properties: Application to thin-film fracture and soil desiccation, Comput. Methods Appl. Mech. Engrg. 368 (2020) 113106, http://dx.doi.org/10.1016/j.cma.2020.113106.

- [34] Y.-S. Lo, M.J. Borden, K. Ravi-Chandar, C.M. Landis, A phase-field model for fatigue crack growth, J. Mech. Phys. Solids 132 (2019) 103684, http://dx.doi.org/10.1016/j.imps.2019.103684.
- [35] K.M. Hamdia, M.A. Msekh, M. Silani, N. Vu-Bac, X. Zhuang, T. Nguyen-Thoi, T. Rabczuk, Uncertainty quantification of the fracture properties of polymeric nanocomposites based on phase field modeling, Compos. Struct. 133 (2015) 1177–1190, http://dx.doi.org/10.1016/j.compstruct.2015.08.051.
- [36] J. Wu, C. McAuliffe, H. Waisman, G. Deodatis, Stochastic analysis of polymer composites rupture at large deformations modeled by a phase field method, Comput. Methods Appl. Mech. Engrg. 312 (2016) 596–634. http://dx.doi.org/10.1016/j.cma.2016.06.010.
- [37] D.-A. Hun, J. Guilleminot, J. Yvonnet, M. Bornert, Stochastic multiscale modeling of crack propagation in random heterogeneous media, Internat. J. Numer. Methods Engrg. 119 (13) (2019) 1325–1344, http://dx.doi.org/10.1002/nme.6093.
- [38] C. Peco, Y. Liu, C. Rhea, J. Dolbow, Models and simulations of surfactant-driven fracture in particle rafts, Int. J. Solids Struct. 156 (2019) 194–209, http://dx.doi.org/10.1016/j.ijsolstr.2018.08.014.
- [39] A. Khodadadian, N. Noii, M. Parvizi, M. Abbaszadeh, T. Wick, C. Heitzinger, A Bayesian estimation method for variational phase-field fracture problems, Comput. Mech. 66 (2020) 827–849, http://dx.doi.org/10.1007/s00466-020-01876-4.
- [40] T. Wu, B. Rosić, L. De Lorenzis, H.G. Matthies, Parameter identification for phase-field modeling of fracture: A Bayesian approach with sampling-free update, Comput. Mech. 67 (2021) 435–453, http://dx.doi.org/10.1007/s00466-020-01942-x.
- [41] N. Noii, A. Khodadadian, J. Ulloa, F. Aldakheel, T. Wick, S. François, P. Wriggers, Bayesian inversion for unified ductile phase-field fracture, Comput. Mech. 68 (4) (2021) 943–980, http://dx.doi.org/10.1007/s00466-021-02054-w.
- [42] S. Nagaraja, U. Römer, H.G. Matthies, L. De Lorenzis, Deterministic and stochastic phase-field modeling of anisotropic brittle fracture, Comput. Methods Appl. Mech. Engrg. 408 (2023) 115960, http://dx.doi.org/10.1016/j.cma.2023.115960.
- [43] N. Noii, A. Khodadadian, F. Aldakheel, Probabilistic failure mechanisms via Monte Carlo simulations of complex microstructures, Comput. Methods Appl. Mech. Engrg. 399 (2022) 115358, http://dx.doi.org/10.1016/j.cma.2022.115358.
- [44] S.M. Dsouza, Hirshikesh, T.V. Mathew, I.V. Singh, S. Natarajan, A non-intrusive stochastic phase field method for crack propagation in functionally graded materials, Acta Mech. 232 (2021) 2555–2574, http://dx.doi.org/10.1007/s00707-021-02956-z.
- [45] J. Oliver, M. Caicedo, A.E. Huespe, J. Hernández, E. Roubin, Reduced order modeling strategies for computational multiscale fracture, Comput. Methods Appl. Mech. Engrg. 313 (2017) 560–595, http://dx.doi.org/10.1016/j.cma.2016.09.039.
- [46] H. Zhang, J. Guilleminot, A Riemannian stochastic representation for quantifying model uncertainties in molecular dynamics simulations, Comput. Methods Appl. Mech. Engrg. 403 (2023) 115702, http://dx.doi.org/10.1016/j.cma.2022.115702.
- [47] C. Soize, C. Farhat, A nonparametric probabilistic approach for quantifying uncertainties in low-dimensional and high-dimensional nonlinear models, Internat. J. Numer. Methods Engrg. 109 (6) (2017) 837–888. http://dx.doi.org/10.1002/nme.5312.
- [48] C. Soize, C. Farhat, Probabilistic learning for modeling and quantifying model-form uncertainties in nonlinear computational mechanics, Internat. J. Numer. Methods Engrg. 117 (7) (2019) 819–843, http://dx.doi.org/10.1002/nme.5980.
- [49] C. Farhat, R. Tezaur, T. Chapman, P. Avery, C. Soize, Feasible probabilistic learning method for model-form uncertainty quantification in vibration analysis, AIAA J. 57 (11) (2019) 4978–4991, http://dx.doi.org/10.2514/1.J057797.
- [50] H. Wang, J. Guilleminot, C. Soize, Modeling uncertainties in molecular dynamics simulations using a stochastic reduced-order basis, Comput. Methods Appl. Mech. Engrg. 354 (2019) 37–55, http://dx.doi.org/10.1016/j.cma.2019.05.020.
- [51] H. Amor, J.-J. Marigo, C. Maurini, Regularized formulation of the variational brittle fracture with unilateral contact: Numerical experiments, J. Mech. Phys. Solids 57 (8) (2009) 1209–1229, http://dx.doi.org/10.1016/j.jmps.2009.04.011.
- [52] C. Miehe, M. Hofacker, F. Welschinger, A phase field model for rate-independent crack propagation: Robust algorithmic implementation based on operator splits, Comput. Methods Appl. Mech. Engrg. 199 (45–48) (2010) 2765–2778, http://dx.doi.org/10.1016/j.cma.2010.04.011.
- [53] D. Santillán, J.C. Mosquera, L. Cueto-Felgueroso, Phase-field model for brittle fracture. Validation with experimental results and extension to dam engineering problems, Eng. Fract. Mech. 178 (2017) 109–125, http://dx.doi.org/10.1016/j.engfracmech.2017.04.020.
- [54] A. Kumar, B. Bourdin, G.A. Francfort, O. Lopez-Pamies, Revisiting nucleation in the phase-field approach to brittle fracture, J. Mech. Phys. Solids 142 (2020) 104027, http://dx.doi.org/10.1016/j.jmps.2020.104027, URL https://www.sciencedirect.com/science/article/pii/S0022509620302623.
- [55] T. Kadeethum, D. O'malley, F. Ballarin, I. Ang, J.N. Fuhg, N. Bouklas, V.L. Silva, P. Salinas, C.E. Heaney, C.C. Pain, et al., Enhancing high-fidelity nonlinear solver with reduced order model, Sci. Rep. 12 (1) (2022) 20229, http://dx.doi.org/10.1038/s41598-022-22407-6.
- [56] D. Da, Model reduction on 3D fracture resistance design, J. Comput. Phys. 463 (2022) 111274, http://dx.doi.org/10.1016/j.jcp.2022.111274.
- [57] N.-H. Nguyen, V.P. Nguyen, J.-Y. Wu, T.-H.-H. Le, Y. Ding, Mesh-based and meshfree reduced order phase-field models for brittle fracture: One dimensional problems, Materials 12 (11) (2019) 1858, http://dx.doi.org/10.3390/ma12111858.
- [58] R. Zimmermann, Manifold interpolation and model reduction, 2019, arXiv preprint arXiv:1902.06502.
- [59] A. Logg, K.-A. Mardal, G. Wells, Automated Solution of Differential Equations By the Finite Element Method: The FEniCS Book, Vol. 84, Springer Science & Business Media, 2012.